UCLouvain

École polytechnique de Louvain

# Dynamics and aerodynamics of flapping swimmers with dissimilar oscillating kinematics

Author: **Thibault Le Men**
Supervisor: **Philippe Chatelain**
Readers: **Grégoire Winckelmans, Mathieu Duponcheel, Renaud Ronsse**
Academic year 2020–2021
Master [120] in Electro-mechanical Engineering

# Aknowledgements

First and foremost, I would like to thank the support team who supervised my work throughout the year.
My supervisor Philippe Chatelain, who guided me to the right path.
And all the teaching team of the thermodynamics and fluid mechanics department of the Institute of Mechanics, Materials and Civil Engineering, who took the time to listen to the progress and problems of mine and all the students having a master thesis related to the department. Particularly, I thank Ignace Ransquin for his time, his good advice and the monitoring that I received.

Secondly, I would like to thank my family and friends.
They supported me and gave me motivation as perseverance all along this work. It was particularly needed in the context of this academic year. Thank you particularly to Simon Berny, whose rigour was a true example.

I would like to thank my readers, Matthieu Duponcheel, Renaud Ronsse, Grégoire Winckelmans, as well as my supervisor Philippe Chatelain, for the consideration that they gave to this master thesis.

Finally, I would like to thank all other people that helped me to write this research.

# Abstract

Several objectives justify group travel for different species of birds and fishes. A first one is the protection against predators. A second one is the fluid interactions that each individual has with the others in its surroundings. However, it is less clear why groups of animals choose particular configurations to travel.
Recent researches advance that, in a system with two pure plunging flapping swimmers, with a leader in front of a follower, the latter can find stable positions behind the leader. This in the case of two synchronized flapping swimmers, so with identical flapping motion, but also in the case where the follower has a flapping motion with different kinematic parameters. In particular, different amplitude, frequency and/or phase angle.

This master thesis uses the computational fluid dynamics to study numerically the fluid interactions between two flapping swimmers in line in water. It is determined where such stable positions for the follower behind the leader occur, in function of the kinematics. Furthermore, the classical Prandtl lifting line theory is used on the follower to evaluate the forces it undergoes in the wake of the leader. It aims to provide an explanation of the convergence of the follower to these positions.

# Contents

# List of Figures

# Chapter 1

# Introduction

## 1.1 The interest in group travel

Several objectives justify group travel for different species of birds and fishes. Studies from the last century advance that a main purpose is, of course, acting against predators [15]. Another one is that dynamic effects induced by their surrounding neighbours benefit to animals . We often observe the V-shape formation of migratory birds. It is shown that this is the optimal configuration to reduce the energy consumption on the whole group and then increase the maximal range significantly [13] (Figure 1.1). If we focus on fishes it is shown that they optimize their motion's efficiency and then reduce their energy consumption finding a suitable position when schooling and using the flow generated by the other swimming bodies around. By a wave-like flapping motion, fishes perform those interactions within the formation. By this way the maximal range achieved by a school is several times the one reached by a lonely swimmer (two to six [22]). Nevertheless, the reason for a particular configuration within a group to perform optimal thrust through vortices shed around each swimmer is still a current research subject.
Engineering often finds inspiration by biomimetics as in this case for flapping foils. Indeed the idea of wings synchronized with the flow in the surrounding inspire nowadays another ship propulsion system involving horizontal wings with a vertical flapping motion placed below or beside the hull of ships with an actively controlled rotation around the pitch axis [3]. This new system could assist or completely replace the conventional propellers. The system would exploit energy standing in sea waves to optimize the engine's propulsion. Another example is the development of micro air vehicles (MAV) inspired also by the flapping of insect wings. The issue of the understanding of such a phenomenon is then also the development of technologies performing efficient lift and thrust.
That is why we can observe that the interest for fluid dynamics of flapping foils increased particularly around the year 2000. Figure 1.2 illustrates well the evolution of this attention to the subject with the number of studies published by year for the last fifty years.

The fish-swimming is mathematically modeled by Ligthill [12], Wu [25, 26] and Cheng [5]. Those researches used the linear and inviscid theory of unsteady foil flow. Patterns in the wake of the swimmer are considered but it assumes predefined shapes, and it forbids then

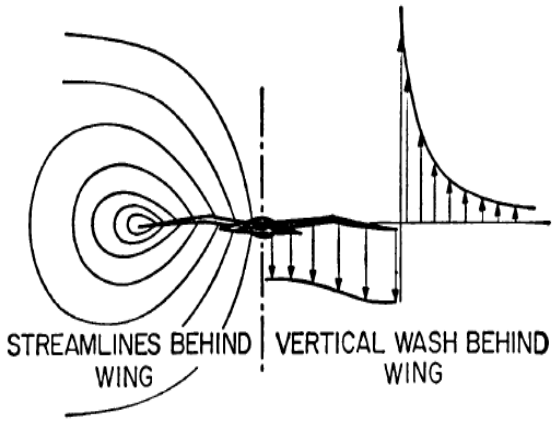


(a) Flow produced by a bird

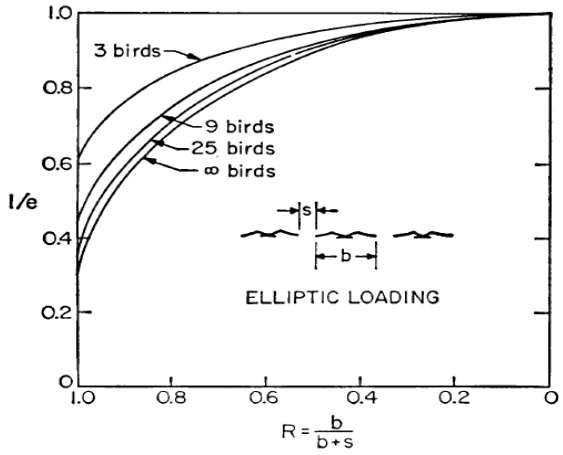


(b) Evolution of the ratio $\frac{l}{e}$, the induced drag in formation on that in solo flight, in function of distance between birds.

Figure 1.1: Birds formation flight. From [13].

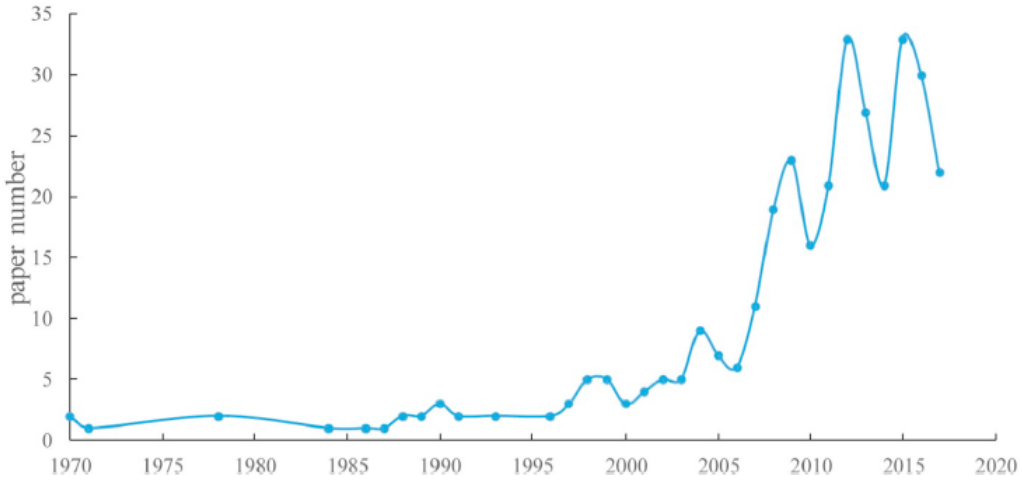


Figure 1.2: Number of papers on flapping foils published by year since 1970. From [27]

these wakes to develop. In 1973 Weihs [22] showed that a school organized in diamond pattern is the optimum configuration for an efficient swim working on hydrodynamics interaction between individual swimmers in a flow still without viscosity. Although Partridge and Pitcher (1979) [14] noticed that most of fish species use other configurations. Weihs and Webbs (1983) [23] concluded that a follower downstream a leader is subjected to greater drag. But Deng (2007) [7] showed that it is not necessarily the case when the follower stands just behind the leader and that the increase or reduction of drag becomes function of the Strouhal number. The importance of the phase difference between the similar kinematics of the two fishes is noticed by Akhtar and Mittal (2005, 2007) [1, 2] to reach equilibrium position. Other school configurations were also studied such as the triangular shape. Chung (2011) [6] studied the performances of a formation made of a leader followed by two followers

side by side in 2-D, and he showed this configuration led to an improved thrust efficiency. All the cited studies assumed that all the swimmers in the group have the same kinematics parameters for the oscillation motion. More recently, Newbolt (2019) [18] studied experimentally the influence of different amplitudes, frequencies and phases between two flapping swimmers in tandem configuration in line. This master thesis aims to reproduce and explain the results provided by Newbolt with a numerical approach with the computational fluid dynamics (CFD). By this way, it will be possible to observe the convergence of the follower to the stable positions as Newbolt [18] did experimentally. But in addition, the numerical approach will allow to evaluate the forces undergone by the follower and then provide an explanation of this convergence to particular positions, in functions of kinematic parameters.

The purpose of this master thesis is then the numerical study of the dynamic behavior of a tandem of flapping swimmers, to understand the synchronization of schooling in water.

In the remaining content, the following sections of Chapter 1 introduce the motion of a real flapping swimmer, the vorticity in the wake that it develops. Then we illustrate the observations and results obtained in the study of tandem fish configuration. Finally the configuration considered for the simulations is introduced.

Chapters 2 develops the tools used. Firstly, the Prandtl lifting line theory is used to compute forces undergone by the follower in a tandem configuration. Secondly, the software Robotran, and the theory behind it, is used to compute the kinematics of the system. And thirdly, the VPM software is used to solve the Navier-Stokes equations around the swimmers.

Chapter 3 presents the results of the simulations that mimic numerically the experiments carried out by Newbolt [18], and compare the results between the experimental and numerical methods. In a second time, the approach of the lifting line theory is applied on the follower swimmer in function of the flow performed by the leader.

At last a final discussion about the presented results and potential avenues for further studies stands in Chapter 4.

## 1.2 The wake behind a flapping swimmer

Obviously the steady motion of a swimmer is complex considering all the undulation along the body in flow direction (Figure 1.3). The classical approach of studies on undulating animals is to consider the motion of a rigid body having a plunging and/or pitching motion, meaning respectively a translation in vertical direction and a rotation in pitch rotation (Figure 1.4). Of course the combined oscillation mode is the closest to a real animal's propulsion system. But taking only plunge motion is sufficient to produce important thrust (see below). Pure pitch motion seems to be the poorest choice for thrust production needing high frequency range to produce any thrust (Figure 1.5a). If we combine the two motions expressed as sinusoidal oscillations, better efficiency and thrust are predicted [16] (Figure 1.5b). These performances are reduced when the two motions are not synchronized anymore.

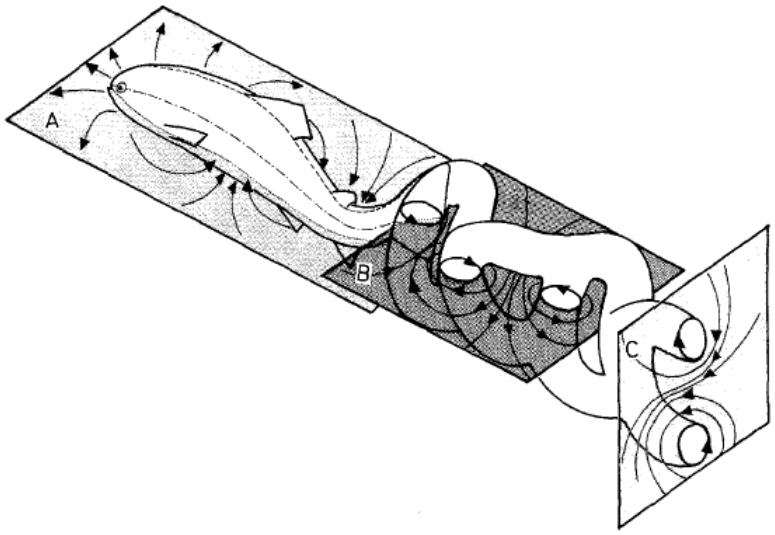


Figure 1.3: General flow pattern around a fish. A) Flow at swimmer level. B) Vortex street establishment. C) Established vortices and vortex rings. From [4].

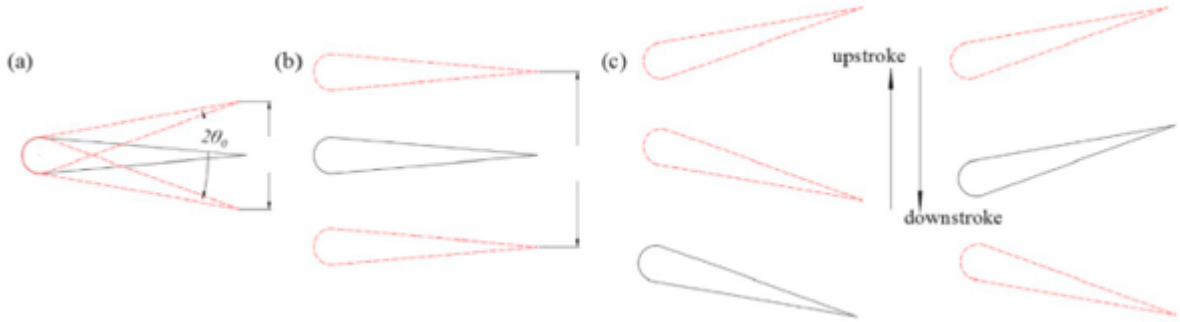


Figure 1.4: (a) pitching motion, (b) plunging motion,(c) complete flapping motion. From [27].

When we observe a two-dimensional flow passed a cylinder in two dimensions, a classical result is the establishment of the von Karman vortex street in the cylinder's wake. This pattern is due to the cylinder shedding vortices of alternating rotation, positive and negative, in its wake. For a three-dimensional flow, a finite span produces additional vortices at the tips of the wing. It can be observed that the wake develops to form vortex rings (as in Figure 1.3). The same phenomena is produced by a flapping swimmer. The boundary layer established along the swimmer's body rolls up and detaches from its trailing edge. Figure 1.6 illustrates the vortices in the 2D-wake of a flapping foil with pure plunging motion for increasing Strouhal number ($St$) values. Indeed the kinematics of flapping foils often are characterized in researches by the Strouhal number based on the oscillation amplitude, or similarly by the reduced frequency $k$:

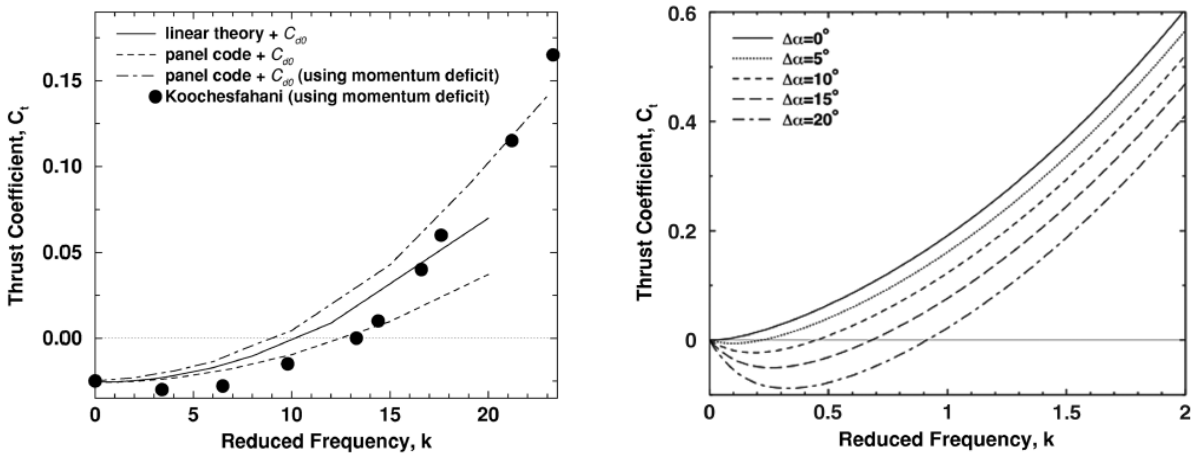


(a) Pure pitch motion

(b) Pitch and plunge combined motion

Figure 1.5: Adimensional thrust coefficient evolution with reduced frequency. From [16]

$$St = \frac{Af}{U} = \frac{1}{2\pi}\frac{A}{c}k \tag{1.1}$$

$$k = \frac{2\pi f c}{U} \tag{1.2}$$

With then:

- $A$, the peak to peak amplitude of oscillation
- $f$, the frequency of oscillation
- $U$, the cruising speed (average speed on a period).
- $c$, the wing's chord.

For a vertical oscillating swimmer and for low $St$, vortices with negative vorticity stand on the upper part of the flow and the vortices with positive vorticity travel on the lower part. Because of this specific pattern a negative momentum area appears in the wake which induces a positive drag force on the swimmer. If we increase $St$, the vortices tend to align with the swimmer. For a specific value of $St$ all the vortices stand in one row and the drag force on the swimmer's body is canceled ($St = 0.13$ according to [11]). Then if we keep increasing $St$, vortices inverse their initial configuration. Upper vortices have now positive vorticity and lower ones have negative vorticity. The wake transformed into the reverse von Karman pattern and the drag force is now negative producing then a trust force on the foil. Animals attempt naturally to reduce their muscle activities keeping a high efficient motion to produce the needed thrust. Strouhal number values of $0.2-0.25$ are the most encountered in biological locomotion. [18, 9, 21]. Reverse von Karman vortex street are then achieved with those values.

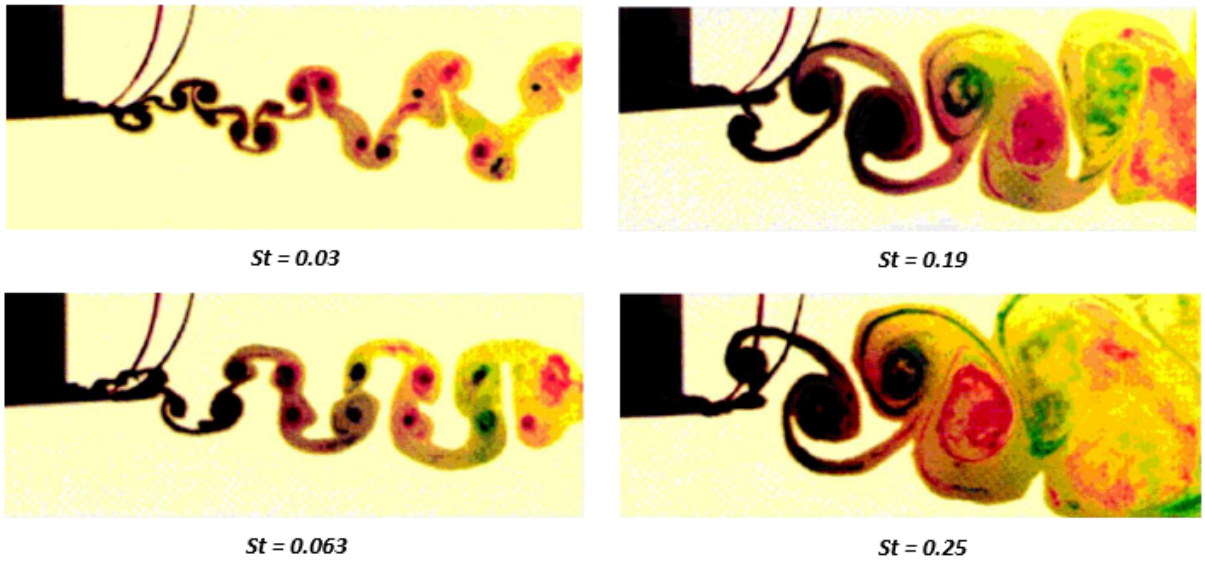


Figure 1.6: Evolution of classical to reverse von Karman vortex street for increasing Strouhal number. From [11].

## 1.3 Tandem configuration

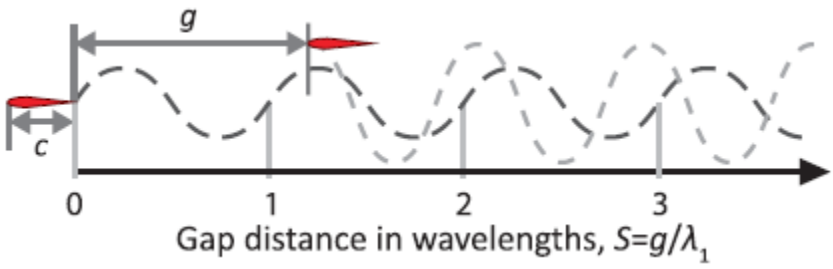


Figure 1.7: Tandem configuration with pure plunging motion. From [18].

The idea in the configuration where a follower is placed in the wake behind a leader, is that the follower can use the vortices in the reverse von Karman vortex street shed by its front neighbour to reduce its muscle activity while maintaining roughly the distance separating both swimmers, the gap distance $S$. And vice versa the leader could enjoy the presence of an active follower reducing its drag. Recent studies show that swimmers with identical kinematics motion synchronize for discrete value of gap distance. Defined starting gap distances evolve to those discrete positions, enumerated by roman numbers, with time on Figure 1.8. The letters a and b show two different evolution paths.
It can be observed that position I is small enough to consider that both wings behave like one. Indeed the reverse von Karman vortex street is not yet developed between the tandem but after the follower. For other equilibrium positions, the reverse vortex street between the wings looks identical to the case with a unique swimmer, traducing a minor influence on the leader. It is no longer true behind the follower where the vortical structures diverge from

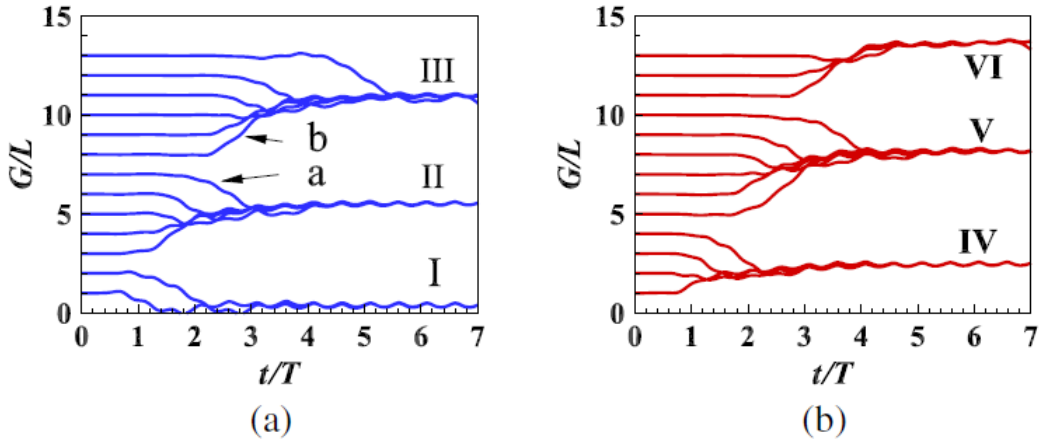


Figure 1.8: Gap distance (here G), divided by the wing's chord (here L), in function of time. (a) Wings in phase, (b) Wings in opposition of phase ($\phi = \pi$). From [28].

the classical reverse vortex street.
Zhu [28] concludes that those stable positions were indeed closely related to the vortex street behind the follower and that the optimal trajectory for the follower is to swim through the vortex with successively opposite sign.
The work of Newbolt (2019) [18] showed experimentally than, even if different kinematics parameters for the two swimmers were considered, the follower can find stable positions behind the leader.

### 1.3.1 Description of the configuration studied

In the present research, the experimentation of Newbolt is repeated using the CFD. The configuration for the simulations is the following :

We consider two 3-D wings in a flow with imposed horizontal velocity (in Z direction). These wings are only free to move in the flow direction and then progress against the inflow. So the three rotations are blocked as well as the translation in Y direction (see Figure 1.9a and 1.9b). Furthermore, the motion in the vertical direction (X axis) is imposed and governed by Equation 1.3 (quantities with index 1 and 2 correspond respectively to the leader and the follower).

$$x_1(t) = \frac{A_1}{2}\sin(2\pi f_1 t) \qquad x_2(t) = \frac{A_2}{2}\sin(2\pi f_2 t - \phi) \tag{1.3}$$

With:

- $f_i$, the frequency.
- $A_i$, the amplitude peak to peak.

- t, the time.
- $\phi$, the phase angle. of the follower with reference to the follower.

The evolution of the gap distance $g$ is then observed over time to detect if any stable position behind the leader is chosen.

In summary, two wings are considered with an imposed motion in the vertical direction and they are free to move horizontally in the inflow direction.

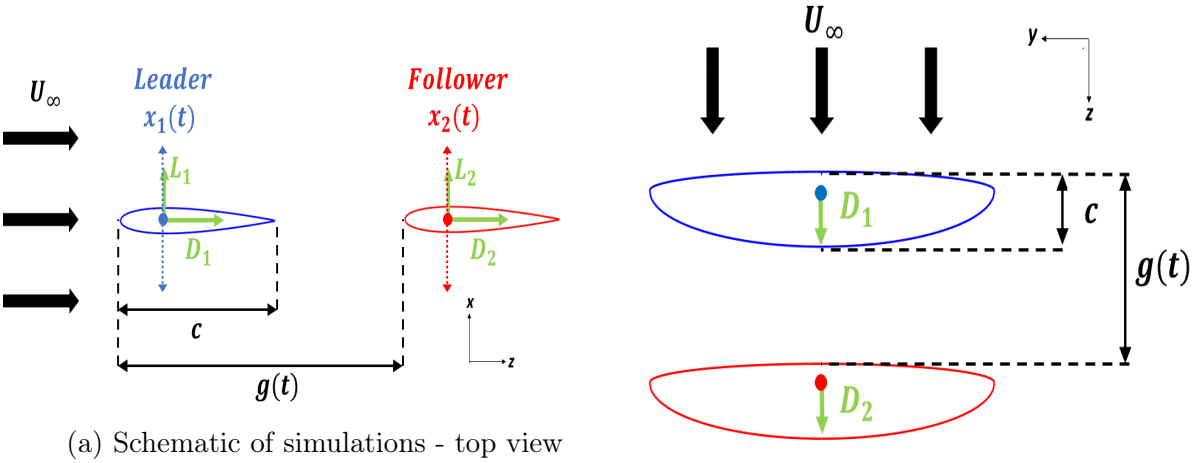


(a) Schematic of simulations - top view

(b) Schematic of simulations - top view

Figure 1.9: Adimensional thrust coefficient evolution with reduced frequency. From [16]

# Chapter 2

# Tools and methodology

At the end of Chapter 1 was introduced the studied configuration for this research. The purpose of the simulation is to compute the flow for that configuration using the vortex particle-meshed method. The latter uses the theory of the lifting line to model any body in a mesh. VPM, which solves the flow, is then coupled with the Robotran software. The latter is used to implement the kinematics of the wings.
In this chapter, we develop each concept used in the above process. We describe the Prandtl lifting line theory, the dynamics handled by Robotran and the equation solved by VPM. Finally, a detailed description of the simulation setup is given

## 2.1 The Prandtl lifting line theory

The Prandtl lifting line theory is an approximated model predicting the circulation on a 3-D wing in function of its configuration, and the velocity of the inflow. This model is valid for 3-D slender wings with large aspect ratio ($A_R > 8$), with small angles of attack (see Figure 2.1 for the definition of wing's geometry) and in an incompressible flow.
This theory models the wing as a line binding the aerodynamic center of every cross section of the wing along the span. The aerodynamic center being the point where the moment of aerodynamic forces are constant and this point stands in most of wings at a quarter of the chord from the leading edge . This line is split in span direction and each element is assumed to behave as a 2-D element. This implies that any tangential velocity has no effect for the computation of the lifting line. It is assumed that the wake behind the wing is not rolling up at the tips of the wing but remains flat. Actually the wake is then a semi infinite flat vortex sheet. It is also imposed that the circulation is zero at the tips of the wing (Figure 2.2).
The shed vortex sheet in the wake induces a vertical velocity component on the lifting line, called the downwashed velocity $w$. This velocity is computed by using the Biot-Savart law. Its expression becomes:

$$w = -\frac{1}{4\pi}\int_{\frac{-b}{2}}^{\frac{b}{2}} \frac{1}{y-y'}\frac{d\Gamma(y')}{dy'}dy' \tag{2.1}$$

Because of the downwash velocity, the total velocity vector is slightly tilted. This adds an extra angle $\epsilon$ to the geometry of the problem. The effective angle of attack is then defined as $\alpha_e = \alpha - \epsilon$. The definition of the circulation, the characteristics of every cross section of the

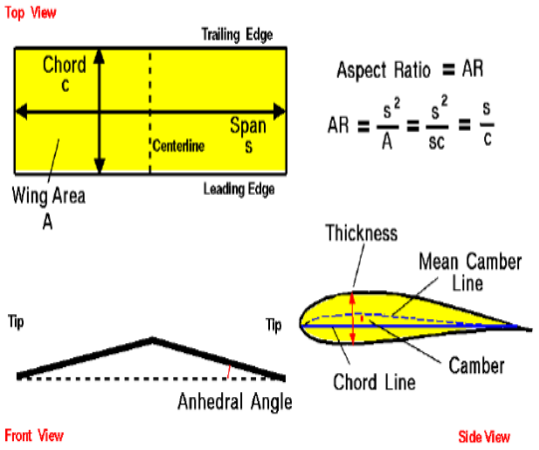


Figure 2.1: Wing geometry definition. From [20].

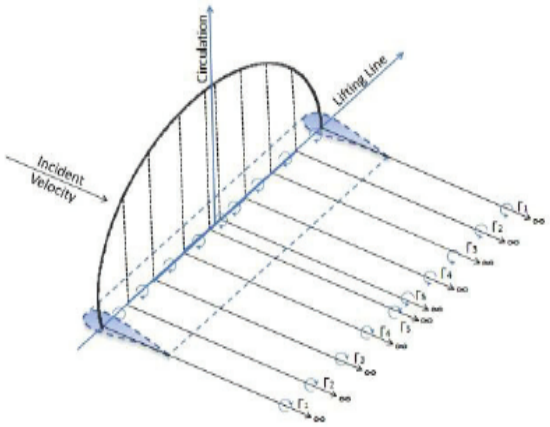


Figure 2.2: Lifting line theory scheme. From [8].

wing in span direction in the case of small angle of attack ($\simeq$), as well as the Kutta-Joukowsky theorem binding circulation and lift, are expressed as:

$$\Gamma = \oint_C u \cdot dl = \int_S \omega \cdot n ds \tag{2.2}$$

$$C_l(y) = \frac{l(y)}{\frac{1}{2}\rho U_\infty^2 c(y)} \simeq a_0(y)\alpha_e(y) \tag{2.3}$$

$$\alpha_e(y) = \alpha(y) - \epsilon(y) \simeq \alpha(y) - \left(\frac{w(y)}{U_\infty(y)}\right) \tag{2.4}$$

$$l(y) = \rho U_\infty(y)\Gamma(y) \tag{2.5}$$

Where $a_0(y) = \frac{dCl(y)}{d\alpha}$. The expression for the circulation $\Gamma(y)$ is derived from Equations 2.2 to 2.5:

$$\Gamma(y) = \frac{1}{2}a_0(y)c(y)U_\infty \left[\alpha(y) - \frac{1}{4\pi U_\infty}\int_{-\frac{b}{2}}^{\frac{b}{2}} \frac{1}{y-y'}\frac{d\Gamma}{dy'}(y')dy'\right] \tag{2.6}$$

An interesting way to approach Equation 2.6 is the following. We use the change of variable $y(\theta) = \frac{b}{2}\cos\theta$ and consider the expression of circulation as a Fourier series :

$$\begin{aligned}\Gamma(\theta) &= U_\infty b \sum_{n=1}^{\infty} B_n \sin n\theta \\ &= \frac{1}{2}a_0(\theta)c(\theta)U_\infty \left[\alpha(\theta) - \frac{1}{2}\sum_{n=1}^{\infty} nB_n \frac{\sin n\theta}{\sin\theta}\right]\end{aligned} \tag{2.7}$$

Once the circulation known along the lifting line, it allows to compute the aerodynamic forces in the wind frame. The lift force is directly computed with Kutta-Joukowsky theorem (Equation 2.5), and the drag force has two components which are the parasitic drag and

the induced drag. The last one is due to the downwashed velocity tilting the total velocity vector from the upstream velocity one. The lift has then also two components in the wind frame. The one parallel to upstream velocity vector is the so-called induced drag, computed by:

$$d_i(y) = l(y) \sin\left(\alpha(y) - \alpha_e(y)\right) \tag{2.8}$$

The parasitic drag ($d_p$), is the force due to friction between the fluid and the surface of the wing (depending of the gas and surface properties), as well as the aerodynamic resistance to the motion of the object through the fluid, depending of the wing shape. Parasitic and induced drags are related by their adimensional coefficients (also valid for small angles) in 3-D with:

$$C_D = C_{D_p} + C_{D_i} = C_{D_p} + \frac{1}{\pi A_R e} C_L^2 \tag{2.9}$$

With $e$ the Oswald's efficiency. Which is a correction factor reflecting the variation of the drag in function of the lift, with reference to an elliptical distribution of lift which has the lowest value of induced drag.

## 2.2 The kinematic implementation with Robotran

### 2.2.1 Configuration and direct dynamics

The kinematics of the system is managed by the software Robotran. This software considers a multi-body system where bodies are connected by joints corresponding each one to a unique translation or rotation. Each joint has a zero mass and can be fixed by anchor points defining the point of attachment on the bodies "parent" and "son". The relative motion of those joints are described with relative generalized coordinates $(q, \dot{q}, \ddot{q})$. The system is seen as a tree-like structure or a closed-loop structure where each body is initially in the frame of its "parent", so when the generalized coordinate between the two bodies is zero. This reference is represented on Figure 2.3. The first frame defined is the inertial frame.
From each configuration with a known position and velocity $(q(t), \dot{q}(t)))$, the acceleration $\ddot{q}$ is computed considering forces and torques applied on each body. This is the so-called direct dynamics approach. To do so the Newton-Euler equation, gathering one equation for translation and one for rotation, is applied in the following form:

$$M(q, \delta)\ddot{q} + c(q, \dot{q}, \delta, F, T, q) = Q(q, \dot{q}) \tag{2.10}$$

where:

- $\delta$ is a vector gathering the mass, the position of the center of mass and the inertia components of a body.
- M is the mass matrix
- c is a non-linear vector containing the contribution of external forces and torques and gravity terms.

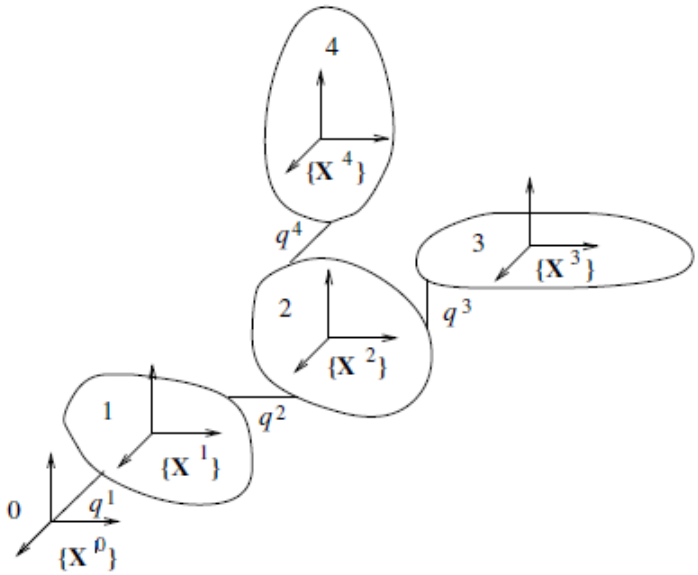


Figure 2.3: Robotran - multibody configuration reference. From [19].

- Q is the vector containing the contribution of the generalized joint forces.

### 2.2.2 Joint forces and external forces

The forces and torques acting on any body of the system are separated in four categories and implemented differently in Equation 2.10.

**The joint force** involved in the vector $Q$ is concentrated in the joint. It could correspond to the suspension on a bike fork for example. The component is along the axis of the joint so in the frame of the "parent" body.

**The gravity force** is considered separately and defined in the inertial frame.

**The link force** is a component of force exerted by a mass-negligible element in the system between two other bodies which are not bound by any joint, like a rod in a car suspension. A link without mass is then implemented where the force acts.

**The external force** is any other force acting on a body of the system. It is applied in one chosen point on the body. But all the external forces and torques acting on a body are gathered in a unique component of force and another of torque acting on the center of mass to be used in Equation 2.10 in vector $c$. This force is implemented in the inertial frame.

## 2.3 The dynamic implementation with the Vortex Particle Meshed approach

### 2.3.1 Vorticity and velocity fields

The computation of the flow uses the vortex method for the resolution of the Navier-Stokes equations (mass conservation and the conservation of momentum). Those in the case of an incompressible flow are, assuming a constant viscosity:

$$\nabla \cdot u = 0 \tag{2.11}$$

$$\frac{\partial \omega}{\partial t} + (\nabla \omega) \cdot u = (\nabla u) \cdot \omega + \nu \nabla^2 \omega \tag{2.12}$$

And the velocity field is computed by the Poisson equation:

$$\nabla^2 u = -\nabla \times \omega \tag{2.13}$$

The method considers firstly a space discretized in particles on which vorticity is computed by previous equations. Then it considers also a mesh where vorticity is interpolated everywhere it is needed from the values computed on the surrounding particles.

### 2.3.2 Lifting line

In an incompressible flow, without the Boussinesq approximation considering small variations of the density $\rho$ due to boillancy effects, the source of vorticity is the friction of the viscous flow with the walls. In the present case, the vortex particle-meshed method does not consider any wall, or friction with it, in the flow but only a lifting line as described in the previous section. Vorticity is also produced when a flow is deflected by the presence of an object in its trajectory. And that will be the only source of vorticity considered in the case of this research.
The theory of the lifting line models any lifting body by a simple line, that is why it is needed to create the vorticity produced by the presence of the body. The theory is then used in an unsteady manner. The circulation is computed at each time step and the vorticity corresponding to the variation of circulation between two time steps is injected in the flow. The effect of the object is well present in the flow without the object being there.

## 2.4 Simulation setup

This section explains how the simulation, using VPM and Robotran, is built. It is used in this study a wing without twist with an elliptical distribution for the chord and an aspect ratio $A_R = 8$ (as said previously $A_R$ has to be significant for a valid model of lifting line). The mean chord is $\overline{c} = 0.04m$ and so the span is $b = 0.32m$. The frame used in VPM is with the Z axis in the flow direction and X axis in the vertical direction pointing upward (Figure 2.4).

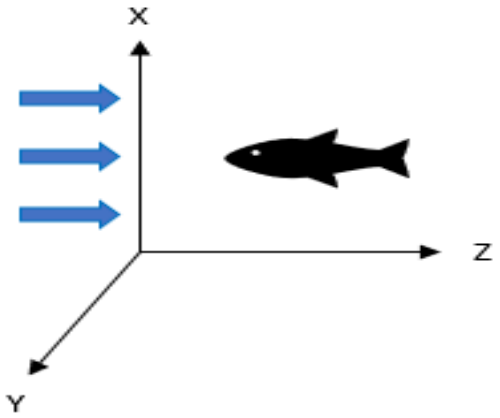


Figure 2.4: Frame considered for the research, with an inflow in blue.

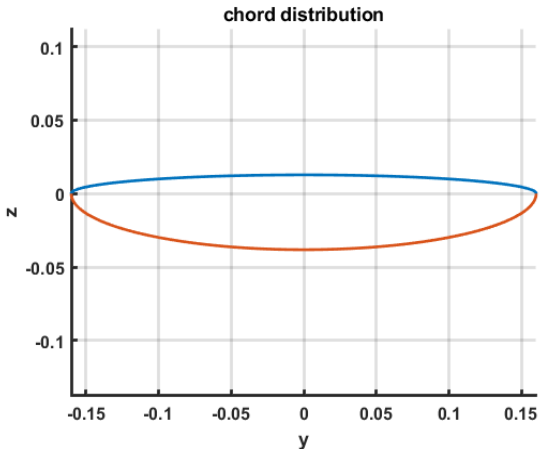


Figure 2.5: Distribution of the chord along the span direction.

The wing has an elliptical distribution of chord along the span (Equation 2.14). This line is described in 150 points linearly distributed and the chord distribution is represented at Figure 2.5. This involves an Oswald's efficiency $e = 1$.

$$c(y) = \frac{4\overline{c}}{\pi}\sqrt{1 - \left(\frac{y}{\frac{b}{2}}\right)^2} \tag{2.14}$$

For all the study, the wing stands in a fluid which is water with density $\rho = 998\frac{kg}{m^3}$ and cinematic viscosity $\nu = 10^{-6}\frac{m^2}{s}$
The wing is modeled in Robotran according to the schematic in Figure 2.6. It is represented by the circle and the rectangle $Body\_1$ is a fictitious body of zero mass needed in the case which all the joints for the wing would be blocked. Robotran demanding at least one independent joint in the system.

| Generalized coordinate | Motion | State |
|---|---|---|
| q1 | Z translation | free |
| q2 | Y translation | blocked |
| q3 | X translation | driven |
| q4 | X rotation | blocked |
| q5 | Y rotation | blocked |
| q6 | Z rotation | blocked |
| q7 | X translation | free |

Table 2.1: Robotran schematic - description

The letters F are the points where forces computed by VPM are applied, implemented as external forces. The left point stands at the center of mass of the wing and the right point, at the aerodynamic center. The current research focus on the gap distance in the flow direction. The generalized coordinates $q_2, q_4, q_5, q_6$ are then blocked, corresponding respectively to the

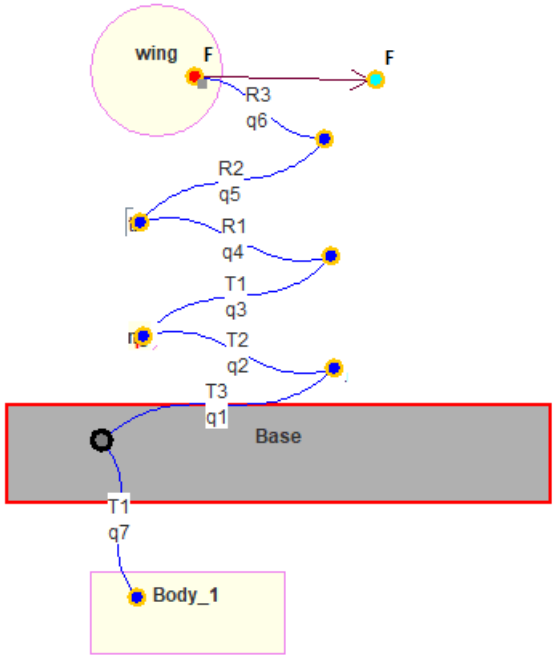


Figure 2.6: schematic of the body system on MbsSysPad - Robotran.

translation on y axis, and the rotation on Z, Y and X axis (see Figure 2.4 and Table 2.1). Translation in Z direction is totally free, and translation in X direction, being the direction of oscillations, is forced with the relation in Equation 1.3. This is then the only forced motion. For the leader wing:

- $f = 2Hz$, the frequency.
- $A = 0.03m$ $(0.75\bar{c})$, the amplitude peak to peak.
- t, the time.
- $\phi = 0$, the phase angle.

All the simulations in VPM use a lifting line discretized in 32 segments per span.
We start from a value for Strouhal number $St = 0.23$ which stands in the most common values for fish propulsion as discussed in Chapter 1. With an amplitude $A = 0.03m$ and a frequency $f = 2Hz$ it gives as an average cruise speed $U_\infty = 0.261\frac{m}{s}$ and then a Reynolds number based on the chord length $Re_c = 10440$.
The simulation is executed in the relative frame of the wing and then an inflow with this velocity and no vorticity is implemented, allowing to conserve a limited volume for the computation of the flow.
The line is considered as a series of 2-D foils. For each foil the classical polar of $2\pi$ for small angles for adimensional lift coefficient are considered $C_l$:

$$\begin{aligned} \frac{dC_l}{d\alpha} &= 2\pi \\ &= a_0 \end{aligned} \tag{2.15}$$

The lift is then defined as well as the induced drag. For the parasitic drag adimensional coefficient, the value is computed such as the wing conserves roughly its position with the inflow implemented, and then respects the Equation 1.1. With $C_d = 0.2$ the stabilization of the position for the wing is obtained (Figure 2.7). The graph (a) shows the position of the wing in wavelength $\lambda$. The graph (b) shows the temporal evolution of the ratio of the speed in the flow direction on the cruising speed, $U_\infty = 0.261\frac{m}{s}$. The time is expressed in periods $\frac{t}{T}$. In this simulation the wing is blocked at its initial position during the two first seconds. It allows to let the flow establish without applying strong constraints on the wing. It is seen that the velocity in the flow direction oscillates around 17% from the cruising velocity $U_\infty$. by a spring force implemented as a joint force.

$$F = -k(L - L_0) \tag{2.16}$$

With $k = 100\frac{N}{m}$ and $L_0 = 0$.

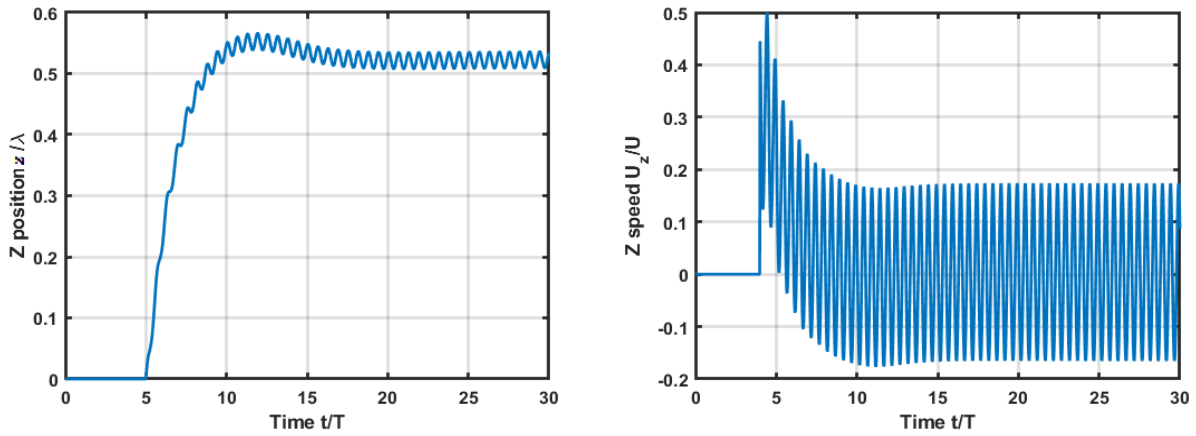


(a) Position of the wing.

(b) Speed of the wing.

Figure 2.7: Stabilization of one wing with inflow.

The motion of the leader is defined and the follower wing has exactly the same configuration than the leader, as well as the same motion imposed. In next chapter the influence of changing the kinematics parameters $A$, $f$, and $\phi$ for the follower's oscillations in Equation 1.3 is studied.

# Chapter 3

# Results and analysis

As said previously, the main purpose of this master thesis is to mimic numerically the experiments of Newbolt [18]. Indeed the CFD provides exact values for forces. This allow to study the evolution of those forces to understand the convergence of the gap distance between the swimmers for precise values of amplitude, phase and frequency in the oscillation motion (Equation 1.3).

In a first time in this chapter, the equilibrium values for the gap distance are studied when the follower phase angle evolves, keeping the amplitude and frequency at constant values. Then the same study is done for different values of amplitude and phase angle, keeping the frequency constant. And finally the influence of the frequency is observed. In a second time, the values of forces that the follower undergoes, computed with the lifting line theory, are compared around equilibrium positions.

## 3.1 Vortex method

The vortex method allows to illustrate the vortex structures developed in chapter 1. Figure 3.1 shows the vorticity developed behind an isolated flapping swimmer moving to the left. The vortex rings are clearly visible. And as it was explained above, vortices with positive vorticity stand in the upper part of the wake, and those with negative vorticity stand in the lower part.
The wing oscillates with the fixed values used for the leader in the rest of this research:

- $A = 0.75\overline{c}$
- $f = 2Hz$
- $St = 0.23$
- $U_\infty = 0.261\frac{m}{s}$

The Figure 3.2 illustrates the vorticity developed by two swimmers. In this simulation, leader and follower have exactly the same kinematics ($\phi = 0$, $\frac{A_2}{A_1} = 1$, $\frac{f_2}{f_1} = 1$), and the second wing

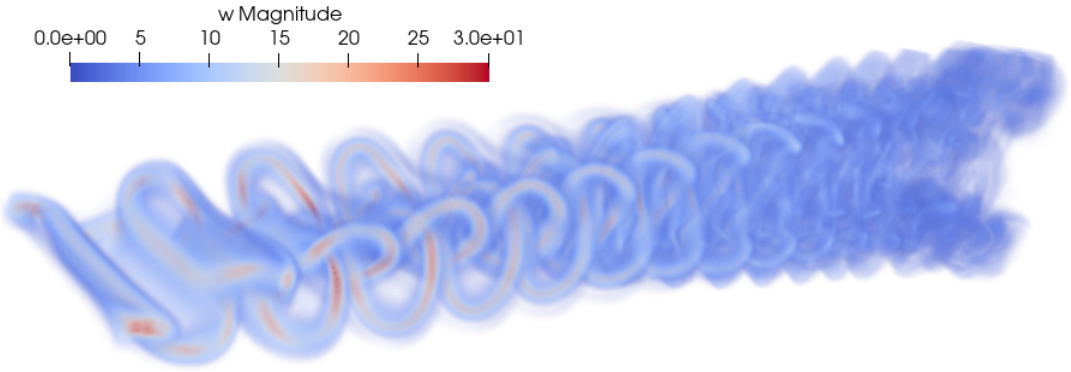


Figure 3.1: Vorticity developed by an isolated flapping swimmer

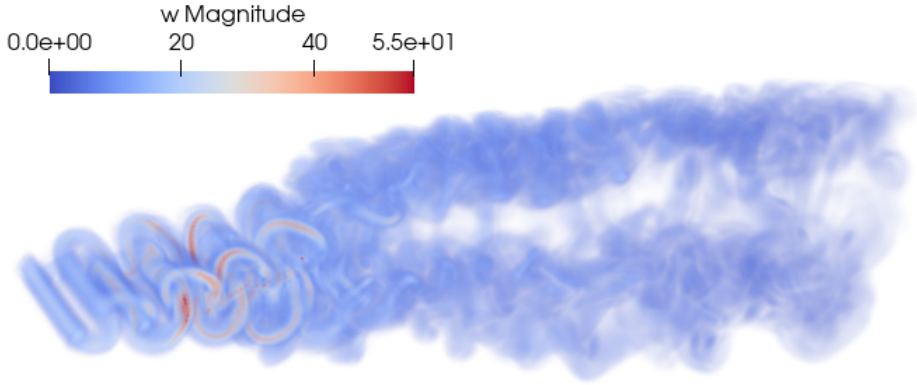


Figure 3.2: Vorticity developed by two synchronized flapping swimmers

stand one wave length behind the leader (it is shown that it is a stable position below). Of course, higher values for vorticity are observed and particularly at the follower position.
The values for the phase angle $\phi$ studied in this section is expressed as a fraction of $2\pi$. For the frequency and amplitude, those are expressed as a ratio between the follower and the leader values, $\frac{f_2}{f_1}$ and $\frac{A_2}{A_1}$ respectively. The position of the follower behind the leader is expressed as a fraction of the leader wavelength:

$$\lambda = \frac{U}{f} \tag{3.1}$$

$$S = \frac{g}{\lambda_1} \tag{3.2}$$

With g the distance between the two swimmers.

### 3.1.1 Influence of phase angle

An increment of $\frac{\Delta\phi}{2\pi} = 0.1$ is considered to observe the evolution of the gap distance at equilibrium. Newbolt determined stable positions for the follower for $S \leq 4$ (Figure 3.3). On this figure, bullets correspond to experimental measures and the solid line is a model built to interpret experimental results.

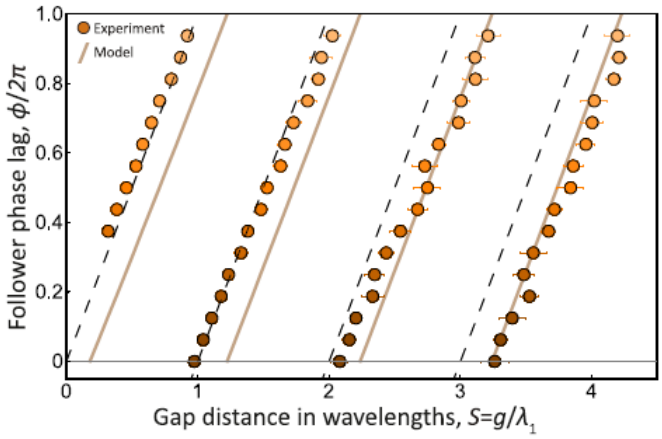


Figure 3.3: Evolution of gap distance with the follower phase angle - From Newbolt [18].

It is observed that the gap distance evolves rather linearly for small values of $S$ ($\frac{\partial S}{\partial(\phi/2\pi)} \approx 1$) and it begins to diverge from this linear evolution around $S = 2$. The vortex approach gives similar results, presented in Figure 3.4. Nevertheless, stable positions for the follower are found even for $S \geq 4$. And the divergence of stable positions with linear evolution with the phase angle is bigger and bigger when $S$ keeps to grow. We observe also for each red bullet a blue interval expressing the standard deviation of the stable position value. Indeed, as observed previously in the stabilization of the wing, each wing oscillates slightly around its position. That induces also an oscillation for the value of S. The Figure 3.5 illustrates a simulation for a specific value of $\frac{\phi}{2\pi} = 0$ with an initial distance of $S_{init} = 1$. The simulation begins with a gap distance close enough to the stable position. Indeed, if the follower is too far behind (ahead) its stable position, the acceleration (deceleration) that it undergoes can lead it to another stable position, roughly at an entire multiple of $\lambda_1$ closer (further) to the leader. It corresponds to an horizontal displacement on Figure 3.4. To avoid it we use a spring force, as said previsouly with Equation 2.16, to keep each wing close to its initial position during the first seconds of simulation.

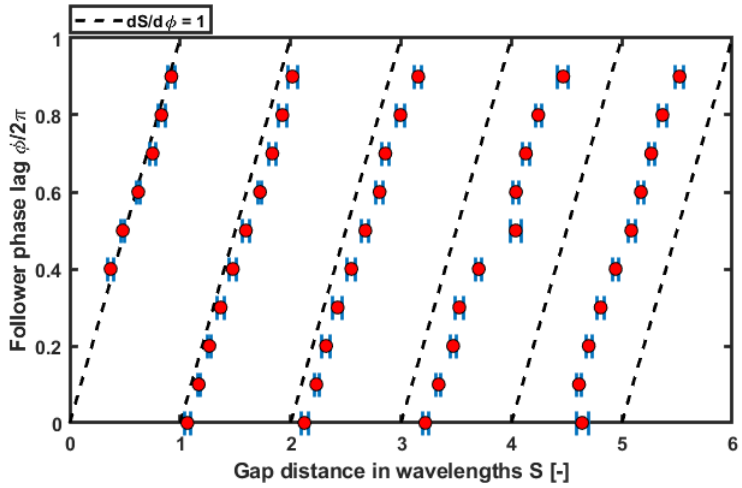


Figure 3.4: Evolution of gap distance with the follower phase gap - VPM

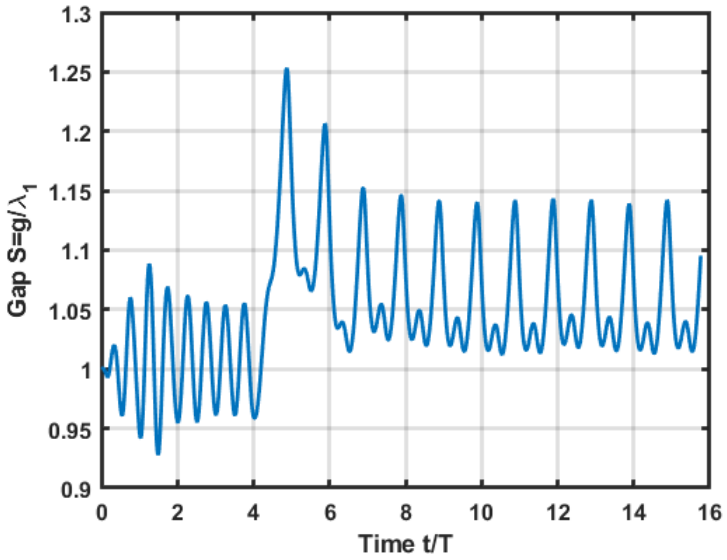


Figure 3.5: Convergence to the stable gap distance $S$ fot: $\frac{f_2}{f_1} = 1$, $\frac{A_2}{A_1} = 1$, $\frac{\phi}{2\pi} = 0$, $S_{initial} = 1$

### 3.1.2 Influence of amplitude

The influence of the ratio $\frac{A_2}{A_1}$ is now studied. To do so, this ratio evolves from 0.2 to 1.8. We will see that values out of this interval do not have any interest. But here with the follower phase angle variation, every value matched a certain stable position for the follower, except for too small values of $S$. With different values of oscillation amplitudes, the follower can find a stable position, reduce this distance with the leader until they collide or, in an opposite way, the follower loses the leader and the distance between the swimmers increases. That is what Newbolt observed in Figure 3.6. One more time, bullets stand for experimental results and the colored surfaces for the predictions of its model. It is remarked that the horizontal line at $\frac{A_2}{A_1} = 1$ corresponds to the previous results. The graph distinguishes three predicted areas where the gap distance is stable, increases or decreases. We obtain the Figure 3.7

numerically where bullets correspond to stable positions, and different colors for values of phase angle. The two curves model the limits of the unstable region predicted in Figure 3.6.

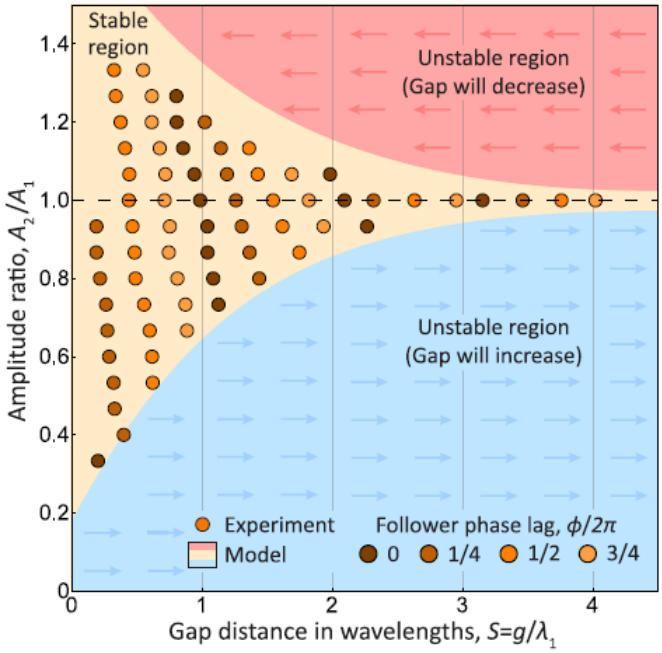


Figure 3.6: Evolution of gap distance with the oscillation amplitude of the follower - Newbolt [18].

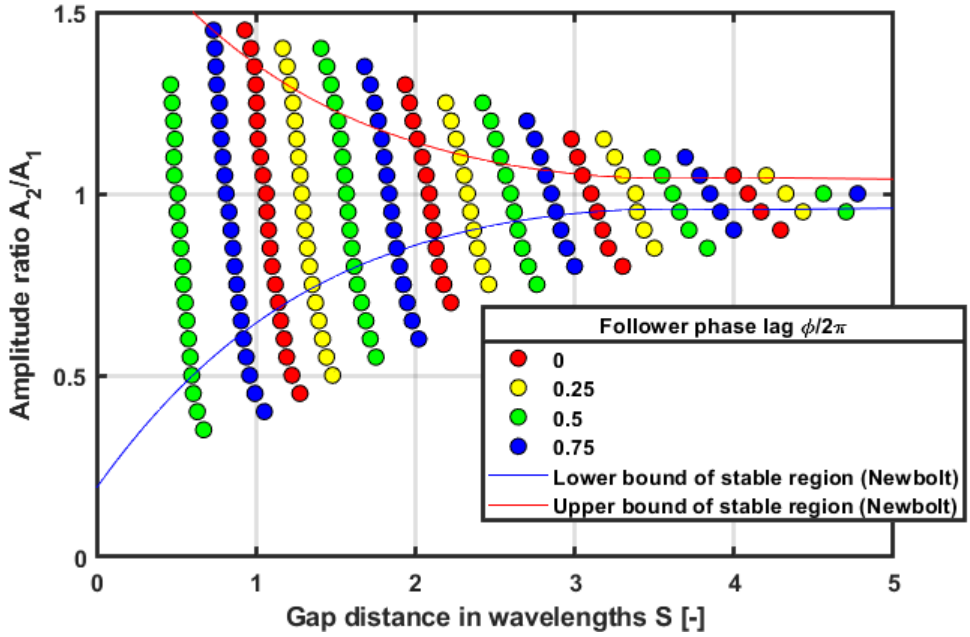


Figure 3.7: Stable gap distance between swimmers with different amplitude ratios $\frac{A_2}{A_1}$ and phase angles $\frac{\phi}{2\pi}$

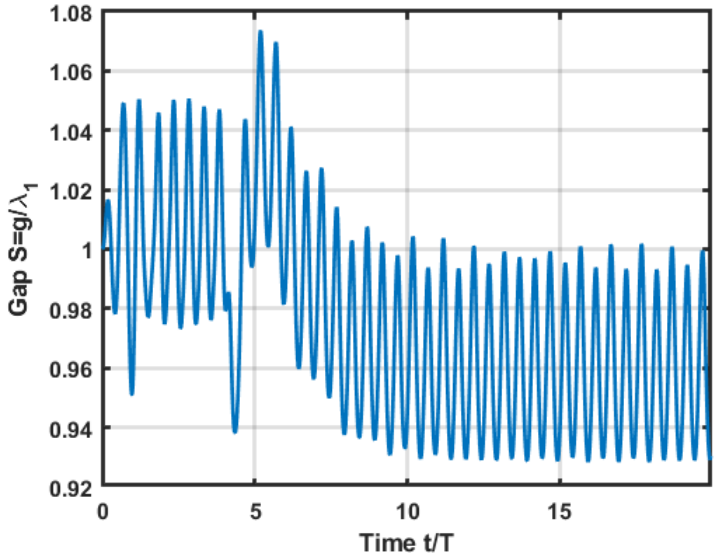


Figure 3.8: Convergence to the stable gap distance $S$ fot: $\frac{f_2}{f_1} = 1$, $\frac{A_2}{A_1} = 0.5$, $\frac{\phi}{2\pi} = 0.75$

Several comments can be done. Firstly, numerical results announce stable positions beyond the limits announced. To find those positions, the simulations started from stable gap distances known by the study of the phase angle with $\frac{A_2}{A_1} = 1$. Then the amplitude ratio increases, or decreases by increment of $\Delta\left(\frac{A_2}{A_1}\right) = 0.05$. If there is no sign of convergence after ten periods, it is considered that no stable position is possible for the actual amplitudes ratio and gap range. Such an evolution is visible at Figure 3.8. Secondly, the variation of $\phi$ has the same effect than in the previous study. Higher values of phase angle increase the gap $S$. A third remark is that stable positions found beyond the limits of Newbolt' study seem to curve, announcing the close divergence to collision or separation. Furthermore a series of points, with different amplitudes ratio and for a particular follower phase angle, get stretched along a bigger range of gap distance $S$ when this last increases. Fourthly, it is more easier for a follower to maintain the gap with amplitudes ratio $\frac{A_2}{A_1} \leq 1$ for low values of $S$. It can be observed indeed that for $S = 1$, the follower can swim at a stable gap with $A_2 = 0.5A_1$, but not with $A_2 = 1.5A_1$.

### 3.1.3 Influence of frequency

In general terms, different frequencies for the two swimmers guide to unstable positions for the follower. As introduced in the previous discussions, this latter will eventually collides or looses the leader. Nevertheless, the change in the frequency ratio reveals two new remarkable areas in the Newbolt research, on Figure 3.9. A main curve on this graph is the curve $A_1 f_1 = A_2 f_2 = 1$. Above this one the swimmers generally collide, and below, separate. But the green area shows the sets of kinematics parameters for which the follower performs stable cycles in gap distance. Those cycles are visible on Figure 3.10. Indeed, the distance $S$ varies by more than one wavelength $\lambda_1$. Those cycles occur for slightly lower frequency ratios and higher amplitude ratios. The second area in purple gathers the set of kinematics parameters for which experimental results of Newbolt perform unstable positions, leading sometimes to collision, sometimes to separation. Despite those results, the two regions are not found using VPM, and the Figure 3.9 is simplified to collision and separation areas, with the stable cycles area guiding to collision (Figure 3.11), and unstable positions area guiding to separation (Figure 3.12).

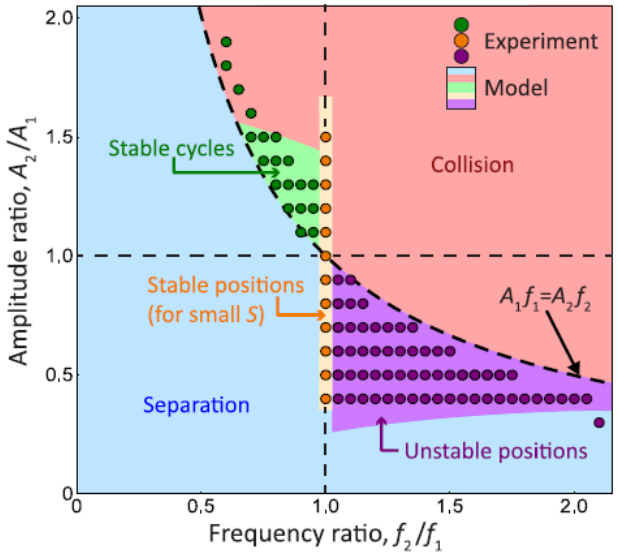


Figure 3.9: Stable gap distance with different amplitude and frequency for the follower oscillations - Newbolt [18].

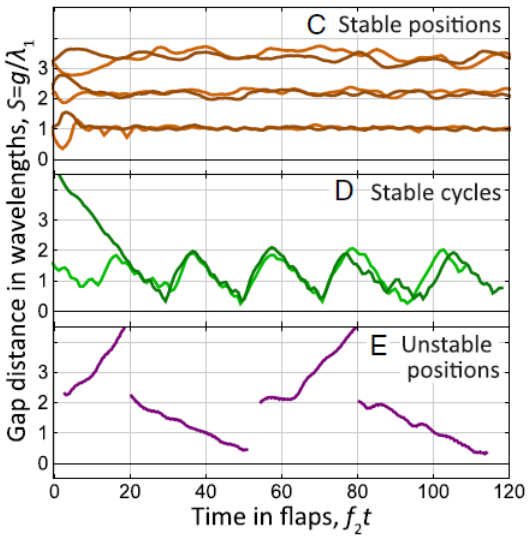


Figure 3.10: Evolution of gap distance $S$ for stable positions (C), stable cycles (D) and unstable positions (E) - From Newbolt [18].

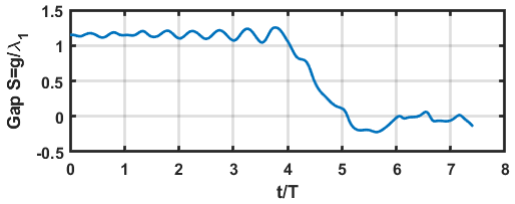


Figure 3.11: Evolution of gap distance $S$ for $\frac{A_2}{A_1} = 0.5$, $\frac{f_2}{f_1} = 1.2$, $\frac{\phi}{2\pi}$=0.

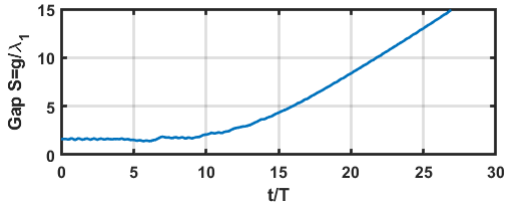


Figure 3.12: Evolution of gap distance $S$ for $\frac{A_2}{A_1} = 0.5$, $\frac{f_2}{f_1} = 1.2$, $\frac{\phi}{2\pi}$=0.

## 3.2 Lifting line theory approach

The previous section showed that a follower can reach several equilibrium positions behind a leader, depending on its kinematic parameters. In this section the Prandtl lifting line theory is used to examined the forces experienced by that follower at a stable position and around it.

### 3.2.1 Circulation and forces at a stable position

In VPM simulations, an inflow is used with the cruising velocity $U_\infty$. When a wing is at equilibrium in flow, the wing then maintains the same position in the flow on average because of this incoming velocity. In other words, the forces acting on a wing at equilibrium are zero on average.
The incoming velocities due to the inflow and the motion of the leader wing are taken from VPM. A stable position for the follower occurs with $\frac{A_2}{A_1} = 1$, $\frac{f_2}{f_1} = 1$ and $\frac{\phi}{2\pi} = 0$ at $S = 1.065$, and this position is taken for the following discussion. The code used to solve the lifting line stands in Appendix A. Figures 3.13 to 3.18 show the evolution of the circulation, the downwash velocity and forces performed by the follower as well as the incoming vertical velocity encountered by the wing.
The quantities measured are observed on two periods $T$ of oscillations along the time axis $\frac{t}{T}$, and this along the span of length $b$.
Lift and drag curves of course look identical because of Equation 2.5. A symmetrical oscillation centered around zeros is well observed. The incoming vertical velocity is consequent for the induced drag that the follower will perform. As a reminder, the Prandtl lifting line theory does not consider any velocity component tangent to the line, only perpendicular components matter, so the velocities in X and Z directions.
The total drag can be computed and is represented on Figure 3.19. If we take the average value on an integer multiple of periods, the obtained value is $\overline{D} = -0.9256N$. It is closed to zero but not equal. Because this position is well defined by VPM as a stable position, this suggests that this residual force could be due to the usage of two different tools for the same problem. Another possibility is the defined accuracy of the tools, as the finite segmentation of the lifting line along the span in VPM. In any case, this residual force, called $F_0$, is considered as an offset in the rest of the following discussion and is removed in the further results, it defines then a zero force at the equilibrium position.
The following sections discuss, as in the first part of this chapter, the influence of the kine-

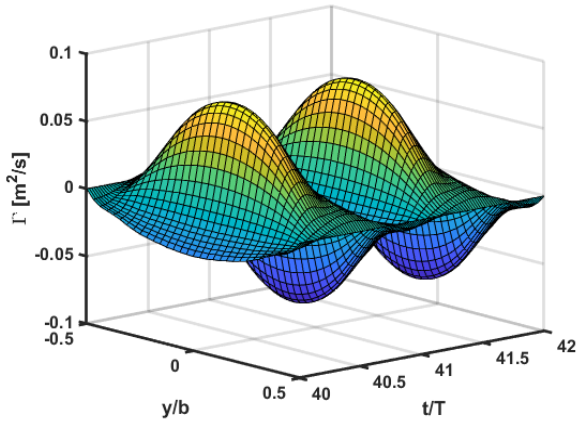


Figure 3.13: Circulation along the span in function of time.

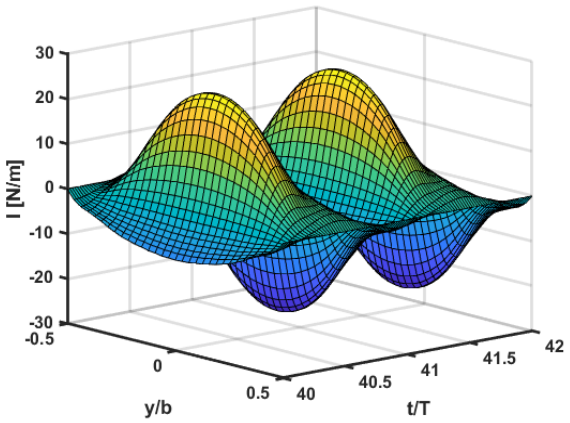


Figure 3.14: Lift per unit length along the span in function of time.

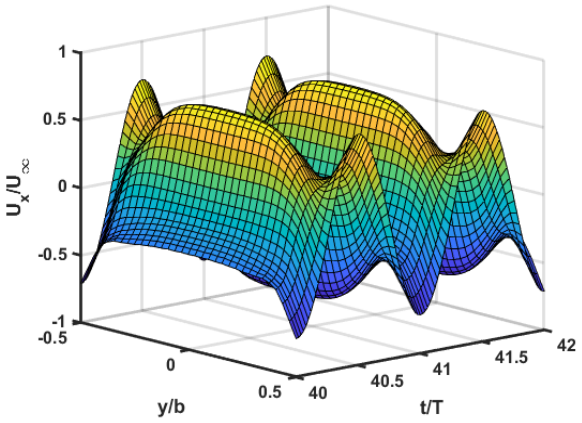


Figure 3.15: Incoming vertical velocity along the span in function of time.

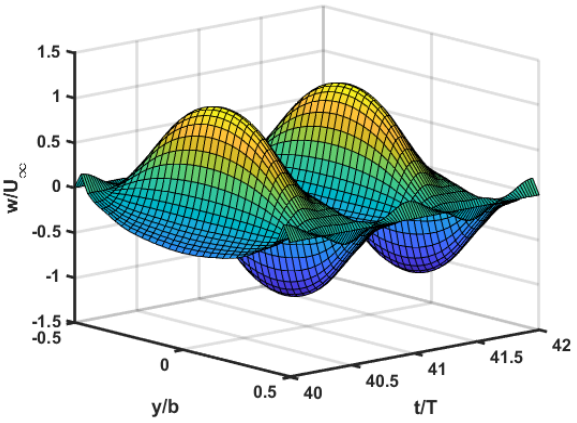


Figure 3.16: Downwash velocity along the span in function of time

matic parameters.

### 3.2.2 Influence of phase angle

Around the equilibrium position described above, the average drag force undergone by the follower are computed for a phase angle $\frac{\phi}{2\pi} = [-0.3, -0.2, -0.1, 0, 0.1, 0.2]$. The results stand on Figure 3.20 on which is shown the average adimensional drag coefficient computed as:

$$C_D = \frac{\overline{D} - F_0}{\frac{1}{2}\rho U_\infty^2 b\overline{c}} \tag{3.3}$$

A negative $C_D$ corresponds to a thrust force, pulling the wing towards the leader. A first comment is that data corresponding to a wing standing at $S = 1.065$ and $S = 1.1$ respectively, are superposed. It suggests that the two positions are too close to each other to perform

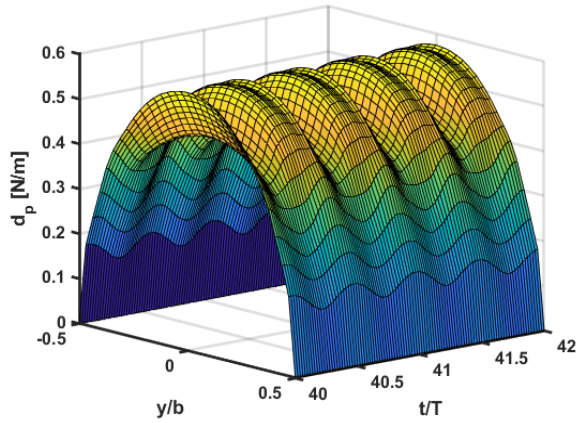


Figure 3.17: Parasitic drag per unit length along the span in function of time.

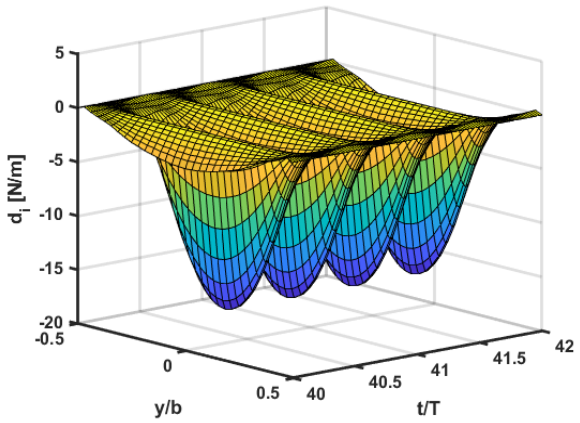


Figure 3.18: Induced drag per unit length along the span in function of time

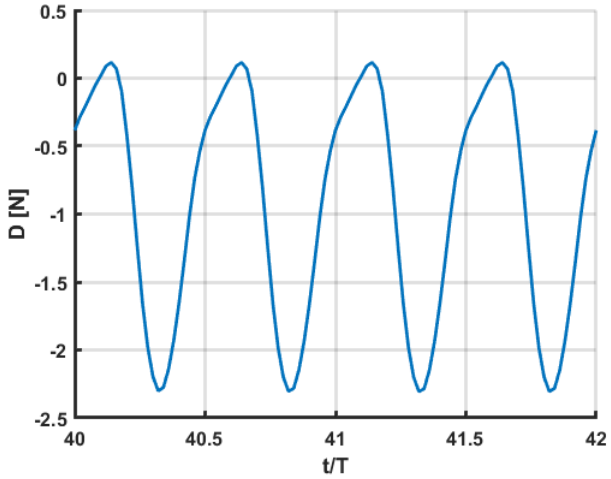


Figure 3.19: Total drag undergone by the wing at the stable position $\frac{A_2}{A_1} = 1$, $\frac{f_2}{f_1} = 1$ and $\frac{\phi}{2\pi} = 0$ at $S = 1.065$

different results by the implemented simulation. Secondly, the stable position is well located at a zero phase angle ($C_D = 0$).
Around the stable position, the results confirm, as it was observed on Figure 3.4, that an increasing phase angle for the follower induces a bigger drag force on it and pushes it backwards. And at the opposite, it pushes it forwards for a decreasing phase angle. If the variation is too important, the evolution of the resulting drag is less obvious. It can be explained by the fact that the stable position for those phase angles stand too far from the studied position, and a more complicated stabilization process takes place.

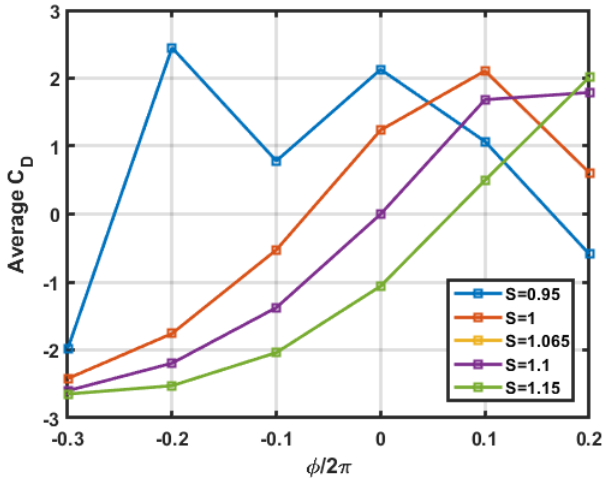


Figure 3.20: Average drag coefficient $C_D$ in function of follower phase angle $\frac{\phi}{2\pi}$ around the equilibrium position at $S = 1.065$

### 3.2.3 Influence of amplitude

The adimensional drag coefficient is observed here for amplitude ratio $\frac{A_2}{A_1} = [0.9, 0.951, 1.05, 1.1]$, and this study is repeated for $\frac{\phi}{2\pi} = [-0.25, 0, 0.25]$.

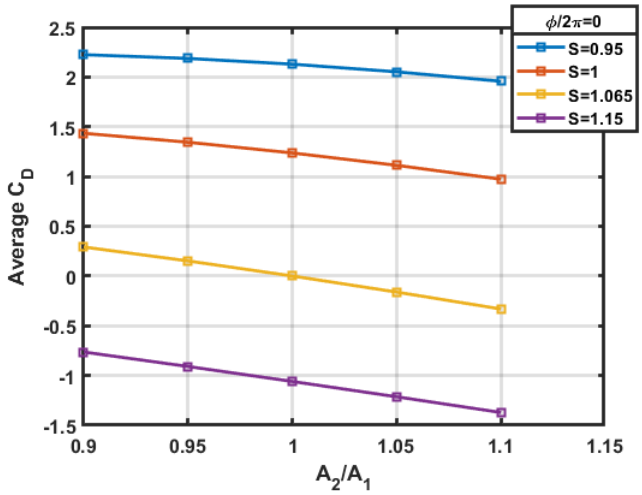


Figure 3.21: Average adimensional drag coefficient, for $\frac{\phi}{2\pi} = 0$, in function of the amplitude ratio.

The Figure 3.7 predicted that higher values for the amplitude ratio, ($\frac{A_2}{A_1} \geq 1$) pull the follower towards the leader, and lower values push it away. That is confirmed by the $C_D$ values shown on Figure 3.21. The same effect is found for a wing standing at different gap distances. More the wing is in front of its stable position, more $C_D$ increases to bring it back to $S = 1.065$. Figures 3.22 and 3.23 show the cases where the phase angle equals $-0.25$ and $0.25$ respectively. Obviously, a zero $C_D$ is not find anymore for $\frac{A_2}{A_1} = 1$ and $S = 1.065$. It illustrates

again the effect of the phase angle discussed above.

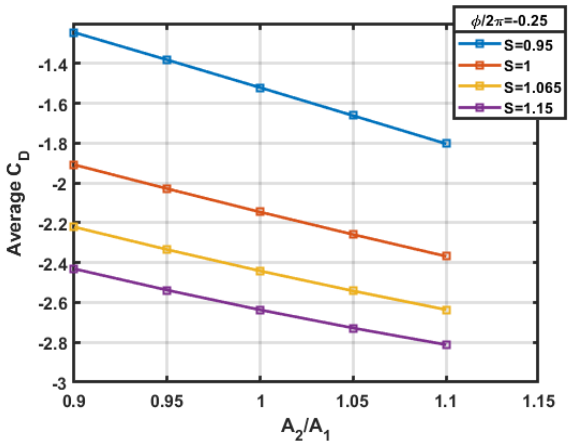


Figure 3.22: Average adimensional drag coefficient, for $\frac{\phi}{2\pi} = -0.25$, in function of the amplitude ratio.

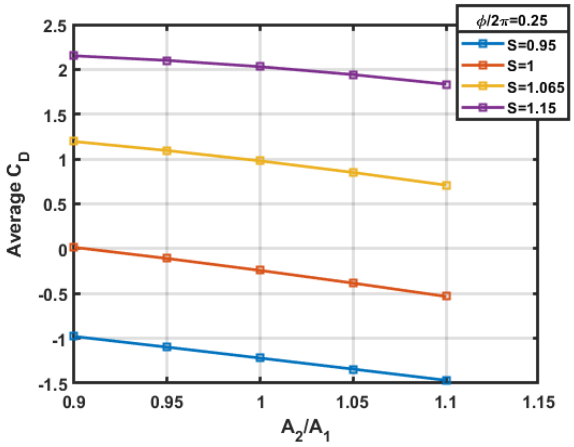


Figure 3.23: Average adimensional drag coefficient, for $\frac{\phi}{2\pi} = 0.25$, in function of the amplitude ratio.

### 3.2.4 Influence of frequency

The adimensional drag coefficient is observed here for frequency ratio $\frac{f_2}{f_1} = [0.9, 0.951, 1.05, 1.1]$, and this study is repeated for amplitude ratio $\frac{A_2}{A_1} = [0.9, 0.95, 1, 1.05, 1.1]$.

For unitary frequency ratio, we find the previous results about $C_D\left(\frac{A_2}{A_1}\right)$.
Figures 3.9 to 3.12 announced that, in general terms at least, a frequency ratio different than one conducts to an unstable gap distance. In the case of an unitary amplitude ratio, The wings collide if the follower has a higher frequency than the leader. Figure 3.24 shows this case, but we observe here that every values for $f_2 \neq f_1$ conducts to negative $C_D$, so a thrust towards the follower. This is in contradiction with the VPM approach. Furthermore, the position of the wing change only slightly this thrust still for $\frac{f_2}{f_1} \neq 1$.

Figures 3.25 to 3.28 show the same study for $\frac{A_2}{A_1} = 0.9, 0.95, 1.05$ and 1.1 respectively, where similar results are obtained. In addition, the negative $C_D$ obtained for $f_2 \neq f_1$ is decreasing again when the amplitude ratio is increasing.

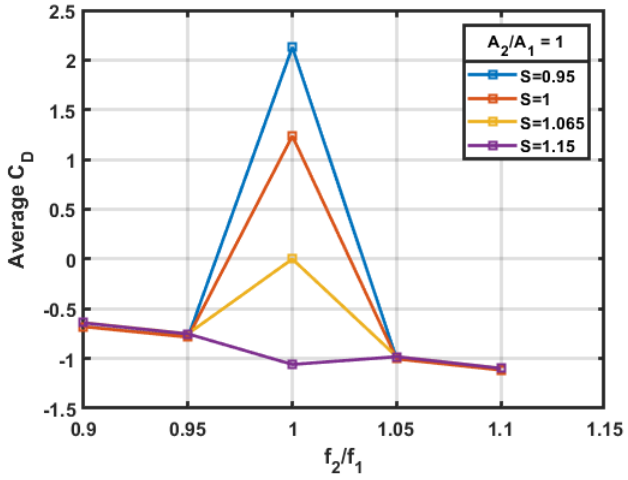


Figure 3.24: Average adimensional drag coefficient, for $\frac{A_2}{A_1} = 1$, in function of the frequency ratio.

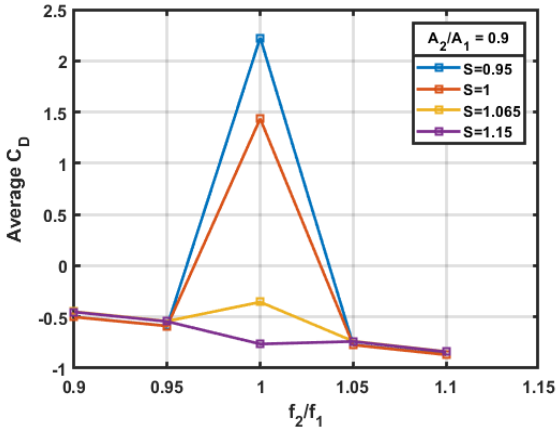


Figure 3.25: Average adimensional drag coefficient, for $\frac{A_2}{A_1} = 0.9$, in function of the frequency ratio.

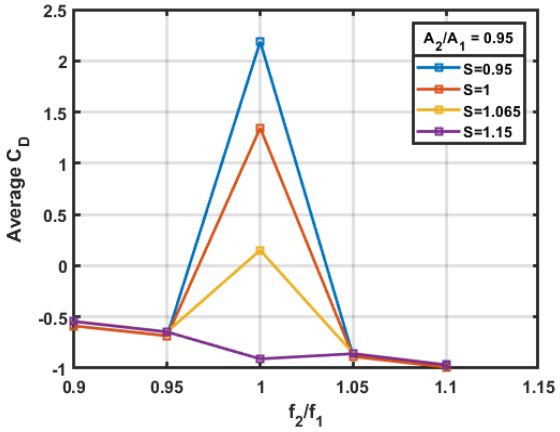


Figure 3.26: Average adimensional drag coefficient, for $\frac{A_2}{A_1} = 0.95$, in function of the frequency ratio.

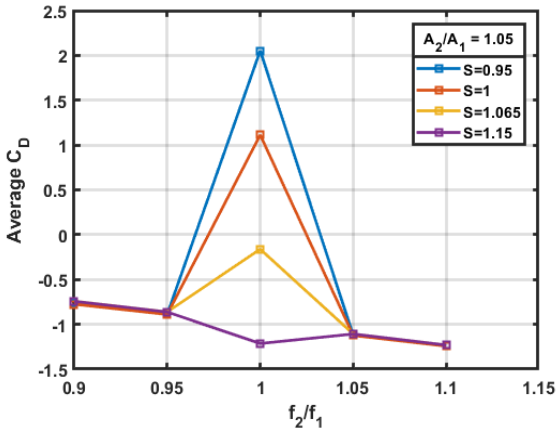


Figure 3.27: Average adimensional drag coefficient, for $\frac{A_2}{A_1} = 1.05$, in function of the frequency ratio.

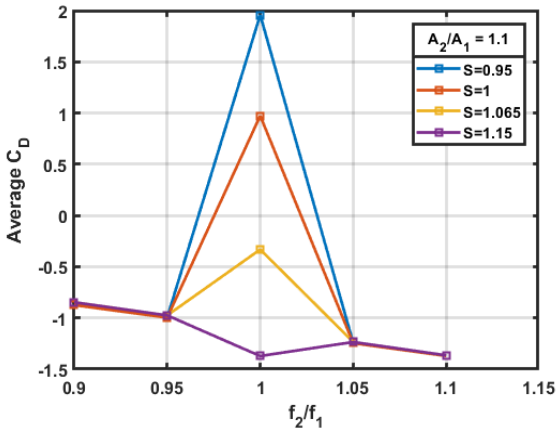


Figure 3.28: Average adimensional drag coefficient, for $\frac{A_2}{A_1} = 1.1$, in function of the frequency ratio.

# Chapter 4

# Conclusion and perspectives

## 4.1 Discussion about the obtained results

This master thesis has two purposes. Firstly, the numerical implementation of a two-body system as Newbolt (2019) [18] did experimentally, determine all the circumstances conducting a flapping swimmer behind a leader to stabilize at certain distances of this latter, and find theses positions. Secondly, the analysis of the forces undergone by a wing at theses stable positions and around to define the explanation of this equilibrium between theses flapping swimmers.

The results of Chapter 3 confirm that swimmers can conserve a stable gap distance, as announced by previous studies ([16, 27, 28]). But also that this event is possible for asynchronous oscillating swimmers, as advanced by Newbolt [18]. This for differential phases between the sinusoidal flapping motion of both the swimmers, but more interestingly, also for different oscillation amplitudes. A follower can then stay close behind a forward leader in the case where it reduces its amplitude flapping by half for example. By this way it could reduce its energy consumption during any travel and increase the maximum range it is able to achieve, as it is known they do when they are schooling [23].

Nevertheless, the influence of the frequency of both swimmers give results that are not reached by the CFD. In particular, The stable cycles obtained by experimentation [18].

By the use of the classical lifting line theory of Prandtl, this research shows how forces evolve at the stable positions, and around, for the follower, and gives an explanation for them. Indeed, the drag force is near to zero for the stable position. The two swimmers achieve to cancel out the additional force that the follower might experience in the wake of the leader.

## 4.2 Avenues for further studies

As explained in the first chapter, the pure plunging motion is the one creating the most amount of thrust [11]. But the closest model to reality for the animal oscillation motion is the combined pitching and plunging motion [27]. A possible further development would be the implementation of this additional motion to the simple vertical oscillation considered in this master thesis.

We have observed here the fluid interactions in a two-body system. But group of animals often are composed by far more individuals. The Figure 4.1 show the gap distance in wavelengths for three synchronized swimmers, and we observe that both the second and the third wings stabilize at certain positions, as it could be expected. One may ask if the third wing will interact in an exactly equivalent way with its two leaders than the second wing does in a two-body system. It is observed already here that the distance between the two last wings is slightly greater than the two first ones.

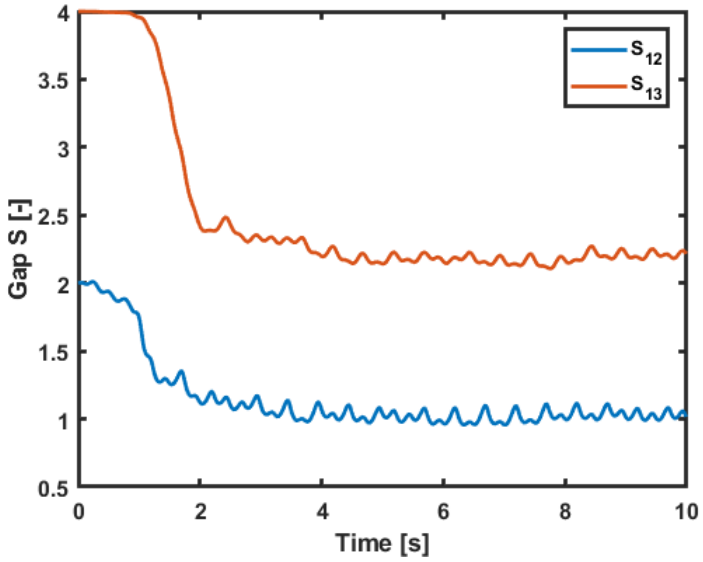


Figure 4.1: Gap distance between three wings. $A_1 = A_2 = A_3$, $f_1 = f_2 = f_3$, $\phi_1 = \phi_2 = \phi_3$. $S_12$ is the gap distance in wavelengths between the first and second wings, $S_13$ is the gap distance in wavelengths between the first and third wings.

# Appendix A

# Lifting line code

```
%Thibault Le Men
%July 2021
%Master thesis - Prandtl lifting line application

close all;
clc;
%clear all vars;

%%
%Parameters

b = 0.32; %Span
AR = 8; %Aspect ratio
a0 = 2*pi; %dCl/d(AoA)
rho = 998; % luid density [kg/m^3]

%Wing shape
%rectangular
%c = @(theta) b/AR;
%e = 0.94; %For AR=8
%elleptical
c = @(theta) 4/pi*b/AR*sin(theta);  %Chord distribution
e = 1; %Oslwald's efficiency

%Number of b_n terms
Nb = 40;

%Number of points for the wing in Y - span direction
Ny = 33;

%Display graphes? 0: no; 1:yes
display = 0;

%AoA of the inflow
```

```
AoA = 5*pi/180*ones(Ny,1);

%Inflow velocity
U = 1*ones(Ny,2); %[Ux Uz]

%Reading H5 files? 0:no 1:yes
reading = 0;

%Start and end time [tstart tend] to consider for the VPM - slices data

tstart = 20;
tend = 40;

% Only odd power of Fourier series ? 0: no; 1:yes
isOdd = 1;

%Follower parameters
Amp = 1*0.03; % [m] p2p amp - frac de A_leader
freq = 0.95*2; % [Hz] fraction de f_leader
phi = 0*2*pi; % x/2pi phase shift

pos = @(t) Amp/2*sin(2*pi*freq*t - phi); % x(t)
Ufx = @(t) Amp*pi*freq*cos(2*pi*freq*t-phi); % x'(t)
Ufz = 0.261; %z(t)
%%
%HDF5 reading from t_start to t_end
if reading
    filename = 'zinstantslice_u_00003_Wing.h5';
    [Uxi, Uyi, Uzi, dx, origins, ends, timei, nb_timei] = readingH5(filename);
end
i_start = 0;
i_end = 0;

for i=1:nb_timei-1
    if abs(timei(i)-tstart)>abs(timei(i+1)-tstart)
        i_start = i+1;
    end
    if abs(timei(i)-tend)>abs(timei(i+1)-tend)
        i_end = i+1;
    end
end
Ux = Uxi(:,:,i_start:i_end);
Uy = Uyi(:,:,i_start:i_end);
Uz = Uzi(:,:,i_start:i_end);
time = timei(i_start:i_end);
nb_time = i_end-i_start+1;
```

```
i_start;
i_end;

%%
%Circulation and forces computation for each i_time

q = @(theta,n) sin(n*theta) + 0.25*a0.*c(theta).*n.*sin(n*theta)./sin(theta)./(b/AR)./AR;
r = @(theta) 0.5*a0.*c(theta)/(b/AR)/AR;

%Computation b_n terms with N = Nb

A = zeros(Nb);
C = zeros(Nb,1);

if isOdd
    for i=0:Nb-1 %i == m %Even terms of n
        ii = 2*i+1;
        C(i+1) = integral(@(theta)q(theta,ii).*r(theta),0,pi/2);

        for j =0:Nb-1 % j == n
            jj = 2*j+1;
            A(i+1,j+1) = integral(@(theta)q(theta,ii).*q(theta,jj),0,pi/2);

        end
    end
else
    for i=1:Nb %i == m %all terms of n
        C(i) = integral(@(theta)q(theta,i).*r(theta),0,pi/2);

        for j =1:Nb % j == n;
            A(i,j) = integral(@(theta)q(theta,i).*q(theta,j),0,pi/2);

        end
    end
end

b_n = A\C; %Coefficients of the Fourier series' terms

theta = linspace(0,pi,Ny);
Gamma = zeros(length(theta),nb_time);
l = zeros(length(theta),nb_time);
di = zeros(length(theta),nb_time);
dp = zeros(length(theta),nb_time);
eps = zeros(length(theta),nb_time);
U_flow = zeros(length(theta),nb_time);
U_xFlow = zeros(length(theta),nb_time);
Di = zeros(1,nb_time);
```

```
Dp = zeros(1,nb_time);
D = zeros(1,nb_time);
w = zeros(length(theta),nb_time);

for t=1:nb_time

    %Getting velocity at the wing position

    %1/ Speed of the follower
    Ufz;
    Ufx(time(t));
    position = [pos(time(t)), 0.0, 0.1305];

    %but pos_x is not obviously on a discretization point of the line:
    position(1) = round(position(1)/dx(1))*dx(1); %Rounded to the closest discret. pnt

    %2/ Speed of the flow at the follower position
    ix = (position(1)-origins(1))/dx(1)+1;
    iy = (position(2)-origins(2))/dx(2)+1;

    Ulx = zeros(Ny,1);
    Ulz = Ulx;

    for i=1:Ny

    %interpolation between the two discret. points around the real
    %position.
    if position(1)-pos(time(t)) > 0

    Ulx(i) = abs((position(1)-pos(time(t)))/dx(1))*Ux(int32(ix-1),int32(iy-(b/2/dx(2))+i-1),t)..
        +(1-abs((position(1)-pos(time(t)))/dx(1)))*Ux(int32(ix),int32(iy-(b/2/dx(2))+i-1),t);
    Ulz(i) = abs((position(1)-pos(time(t)))/dx(1))*Uz(int32(ix-1),int32(iy-(b/2/dx(2))+i-1),t)..
        +(1-abs((position(1)-pos(time(t)))/dx(1)))*Uz(int32(ix),int32(iy-(b/2/dx(2))+i-1),t);;
    else

    Ulx(i) = abs((position(1)-pos(time(t)))/dx(1))*Ux(int32(ix+1),int32(iy-(b/2/dx(2))+i-1),t)..
        +(1-abs((position(1)-pos(time(t)))/dx(1)))*Ux(int32(ix),int32(iy-(b/2/dx(2))+i-1),t);
    Ulz(i) = abs((position(1)-pos(time(t)))/dx(1))*Uz(int32(ix+1),int32(iy-(b/2/dx(2))+i-1),t)..
        +(1-abs((position(1)-pos(time(t)))/dx(1)))*Uz(int32(ix),int32(iy-(b/2/dx(2))+i-1),t);
    end

    U(i,1) = Ulx(i)-Ufx(time(t));
    U(i,2) = Ulz(i);
    AoA(i) = atan(U(i,1)/U(i,2));

    end
```

```
    %Computation of the circulation

    for i =1:length(theta)
        for j = 0:Nb-1

            Gamma(i,t) = Gamma(i,t) + b*b_n(j+1)*AoA(i)*sin((2*j+1)*theta(i));

        end

    end

    %Forces computation
    yy=linspace(-0.16,0.16,Ny);
    chord = 4/pi*0.04.*sqrt(1-(yy./(0.5*b)).^2);

    U_flow(:,t) = sqrt(U(:,1).^2+U(:,2).^2);
    U_xFlow(:,t) = U(:,1);
    l(:,t) = Gamma(:,t).*U_flow(:,t).*rho;

    w(:,t) = Gamma(:,t)./pi./chord' - AoA.*U_flow(:,t);

    if isnan(w(1,t)) || isinf(w(1,t))
        if w(2,t) > 0
            w(1,t) = 0;
        else
            w(1,t) = 0;
        end
    end
    if isnan(w(end,t)) || isinf(w(end,t))
        if w(end-1,t) > 0
            w(end,t) = -0;
        else
            w(end,t) = 0;
        end
    end

    eps(:,t) = atan(-w(:,t)./U_flow(:,t));

    di(:,t) = l(:,t).*sin(eps(:,t));
    Di(t) = sum(di(:,t).*(b/(Ny)));
    dp(:,t) = (0.21*0.5*rho.*(U_flow(:,t)).^2.*chord');
    Dp(t) = sum(dp(:,t).*(b/(Ny)));
    %Dp(t) = 0.21*0.5*rho*b*0.04*mean(U_flow(:,t))^2;
    D(t) = Di(t) + Dp(t);

end
```

```
% mean_drag_i = mean(Di)
% mean_drag_p = mean(Dp)
mean_drag = mean(D)

%%
% Functions implementation

function [Ux, Uy, Uz, dx, origins, ends, time, nb_time] = readingH5(filename)
% readingH5 reads the slices from VPM in the output files filename.h5,
% and build three matrix of dimensions 3; Ux, Uy, Uz beeing respectively
% the x, y and z components of velocity in the simulation space. The fourth
% dimension is time.
% INPUT: -filename; the name of the file.
% OUTPUTS: -Ux, Uy, Uz; the 3D matrices containing the velocity components.
% - dx, the discretization element of the simulation space (dx,dy).
% - origins and ends; the vectors containing respectively two corners of
% the simulation space.
% - time; the vectors containing the time for each instance of velocity.
% - nb_time, the number of instances, so also the length of the third
%dimension of Ux,y,z.

info = h5info(filename); %info du fichier h5

nb_time = h5read(filename,'/nb_time');
%tt = 1:1:nb_time;

dx = h5read(filename,'/geometry/dx')
origins = h5read(filename,'/geometry/origins')
ends = h5read(filename,'/geometry/ends');

time = zeros(nb_time,1);
Ux = zeros(int32((ends(1)-origins(1))/dx(1)+1),(ends(2)-origins(2))/dx(2)+1,nb_time);
Uy = Ux;
Uz = Ux;

for i=1:nb_time

    info_data = info.Datasets(2+i); %info du dataset
    time(i) = info_data.Attributes(2).Value;
    name = "/"+info_data.Name;
    name = char(name);
    rd = h5read(filename,name);
    Ux(:,:,i) = rd(1,:,:);
    Uy(:,:,i) = rd(2,:,:);
    Uz(:,:,i) = rd(3,:,:);
end
end
```

# Bibliography


[1] Akhtar, I. Mittal, R. (2005). A biologically inspired computational study of flow past tandem flapping foils, in: 35th AIAA Fluid Dynamics Conference and Exhibit, Ontario, Canada.

[2] Akhtar, I. Mittal, R. (2007). Hydrodynamics of a biologically inspired tandem flapping foil configuration. Theor. Comput. Fluid Dyn. 21, 155–170.

[3] Belibassakis, K.A. Filippas, E.S. (2015). Ship propulsion in waves by actively controlled flapping foils. Applied Ocean Research, 52, 1-11.

[4] Blickhan, R., Krick, C., Zehren, D., Nachtigall, W., Breithaupt, T. (1992). Generation of a vortex chain in the wake of a suhundulatory swimmer. Naturwissenschaften 79, 220–221.

[5] Cheng, J.Y. Zhuang, L.X. Tong, B.G. (1991). Analysis of swimming of three dimensional waving plates. J. Fluid Mech. 232, 341–355.

[6] Chung, M.H. (2011). Hydrodynamic performance of two-dimensional undulating foils in triangular formation. J. Mech. 27, 177–190.

[7] Deng, J. Shao, X. M. Yu, Z. S. (2007). Hydrodynamic studies on two travelling wavy foils in tandem arrangement. Phys. Fluids 19, 113104.

[8] Epps, B.P. (2010) OpenProp v2.4 Theory Document, MIT Department of Mechanical Engineering Technical Report.

[9] Godoy-Diana, R. Aider, J.L. Wesfreid, J.E. (2008). Transitions in the wake of a flapping foil. Phys Rev E Stat Nonlin Soft Matter Phys. 77.

[10] Khalid, M. S. U. Akhtar, I. Dong, H. (2016). Hydrodynamics of a tandem fish school woth asynchronous undulation of individuals. J. Fluids and Structures. 66, 19-35.

[11] Lai, J. C. S., and Platzer, M. F. (1999). Jet Characteristics of a Plunging Airfoil. AIAA Journal, Vol. 37(12), 1529–1537.

[12] Lighthill, M. (1960). Note on the swimming of slender fish. Journal of Fluid Mechanics, 9(2), 305-317.

[13] Lissaman, P.B.S., Shollenberger, C.A. (1970). Formation flight of birds. Science 168, 1003– 1005.

[14] Partridge, B. L., Pitcher, T. J. (1979). Evidence against a hydrodynamic function for fish schools. Nature 279, 418–419.

[15] Partridge, B. L. (1982). The structure and function of fish schools. Sci Am. J., 246(6), 114-23.

[16] Platzer, M.F., Jones, K.D., Young, J., Lai, J.C.S. (2008). Flapping wing aerodynamics: Progress and challenges. AIAA Journal 46, 2136–2149.

[17] MEED divison, iMMC. UCLouvain. (...). Robotran (Version 1.10) [Logiciel]. Robotran. https://www.robotran.be

[18] Newbolt, J. W., Zhang, J., Ristroph, L. (2019). Flow interactions between uncoordinated flapping swimmers give rise to group cohesion. Proceedings of the National Academy of Sciences of the United States of America, 116(7), 2419-2424.

[19] Robotran. (2018). Modeling multibody systems with Robotran.

[20] Sands, K. (2021, May 10). Wing geometry definition.
Retrieved from https://www.grc.nasa.gov/WWW/Wright/airplane/geom.html.

[21] Triantafyllou, G. S., Triantafyllou, M. S., Grosenbaugh, M.A. (1993). Optimal thrust development in oscillating foils with application to fish propulsion. Journal of Fluids and structures. 7, 205-224.

[22] Weihs, D. (1973). Hydromechanics of Fish Schooling. Nature 241, 290–291.

[23] Weihs, D., Webb, P. W. (1983). Optimization of locomotion. Fish Biomech., 339–371.

[24] Winckelmans, G. (2018). Lifting line theory of Prandtl

[25] Wu, T. (1961). Swimming of a waving plate. Journal of Fluid Mechanics, 10(3), 321-344.

[26] Wu, T. (1971). Hydromechanics of swimming propulsion. Part 3. Swimming and optimum movements of slender fish with side fins. Journal of Fluid Mechanics, 46(3), 545-568.

[27] Xia, W., Zhang, X., Tian, X., Li, X., Lu, W. (2020). A review on fluid dynamics of flapping foils. Ocean Engineering, 195, 106712.

[28] Zhu X., He G., Zhang X. (2014). Flow-mediated interactions between two self-propelled flapping filaments in tandem configuration. Phys Rev Lett 113:238105.

**UNIVERSITÉ CATHOLIQUE DE LOUVAIN**
**École polytechnique de Louvain**
Rue Archimède, 1 bte L6.11.01, 1348 Louvain-la-Neuve, Belgique | **www.uclouvain.be/epl**